

# Locomotion of a multi-link non-holonomic snake robot with passive joints

The International Journal of  
Robotics Research  
2020, Vol. 39(5) 598–616  
© The Author(s) 2020  
Article reuse guidelines:  
sagepub.com/journals-permissions  
DOI: 10.1177/0278364919898503  
journals.sagepub.com/home/ijr  


Tony Dear<sup>1</sup> , Blake Buchanan<sup>2</sup>, Rodrigo Abrajan-Guerrero<sup>3</sup>,  
Scott David Kelly<sup>3</sup>, Matthew Travers<sup>2</sup> and Howie Choset<sup>2</sup>

## Abstract

*Conventional approaches in prescribing controls for locomoting robots assume control over all input degrees of freedom (DOFs). Many robots, such as those with non-holonomic constraints, may not require or even allow for direct command over all DOFs. In particular, a snake robot with more than three links with non-holonomic constraints cannot achieve arbitrary configurations in all of its joints while simultaneously locomoting. For such a system, we assume partial command over a subset of the joints, and allow the rest to evolve according to kinematic chained and dynamic models. Different combinations of actuated and passive joints, as well as joints with dynamic elements such as torsional springs, can drastically change the coupling interactions and stable oscillations of joints. We use tools from nonlinear analysis to understand emergent oscillation modes of various robot configurations and connect them to overall locomotion using geometric mechanics and feedback control for robots that may not fully utilize all available inputs. We also experimentally verify observations and motion planning results on a physical non-holonomic snake robot.*

## Keywords

Geometric mechanics, locomotion, non-holonomic systems, underactuated systems, motion planning

## 1. Introduction

Biologically inspired robots benefit from having a source of inspiration for motion planning, specifically in gaits or locomotion modes. In particular, biological imitation has yielded effective results for snake robot locomotion, which can be achieved by a repertoire of “natural”-looking slithering motions, such as the serpenoid gait described by Hirose (1993). In mechanical imitations of these organisms, we find that variations in robot configuration can lead to a very different set of locomotion “rules” or limitations compared with their biological analogs, such as the amount of control the system can have over its joints. In this article, we consider a robot for which it is impossible to arbitrarily control all of its joints without violating any inherent constraints.

We consider a multi-link snake robot with a configuration shown in Figure 1, where non-holonomic constraints visualized as wheels are placed on each of the links, ensuring that resultant motion only occurs along the link’s longitudinal direction. These constraints can be used to derive relatively simple kinematic models that describe the coupling behaviors among the joints and the overall locomotion of the robot. Although one often assumes control via motors in each individual joint, the kinematic models restrict the combinations of inputs that can be applied, such

as the set of valid input trajectories. The robot is thus often prescribed to follow shapes such as the serpenoid curve in order to avoid singular configurations or those for which the constraints cannot be satisfied exactly.

Unlike much of the previous work analyzing this and related systems, in this article we primarily analyze and control this system by actuating one or two joints while leaving at least one joint unactuated. We show that the actuated joints determine the passive dynamics of this system, contributing to overall locomotion, and show how one may consider gait design to achieve desired motion. This is done in both a kinematic and dynamic context, where the kinematic context assumes two actuated joints and yields a chained form of equations, while the dynamic context allows for the addition of compliance to the joints and

<sup>1</sup>Department of Computer Science, Columbia University, New York, NY, USA

<sup>2</sup>The Robotics Institute, Carnegie Mellon University, Pittsburgh, PA, USA

<sup>3</sup>Department of Mechanical Engineering and Engineering Science, University of North Carolina at Charlotte, Charlotte, NC, USA

## Corresponding author:

Tony Dear, Department of Computer Science, Columbia University, 500 West 120th Street, New York, NY 10027, USA.

Email: tony.dear@columbia.edu

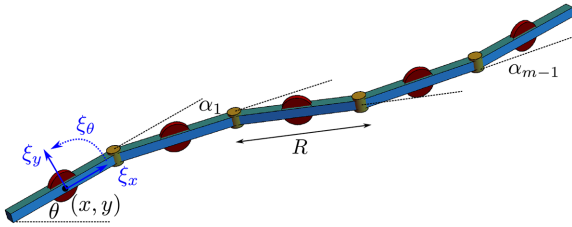


**Fig. 1.** An  $m$ -link non-holonomic snake robot. The coordinates  $(x, y, \theta)$  denote the inertial configuration of the proximal link, which also has body velocities  $(\xi_x, \xi_y, \xi_\theta)$ . Relative joint angles starting from the proximal link are denoted  $(\alpha_1, \dots, \alpha_{m-1})$ .

assumes only one actuated input. We are also able to model the robot's locomotion when passing through singular configurations, which were previously difficult to handle with traditional kinematic models and full actuation of the robot.

The work in this article directly extends that of Dear et al. (2017). The prior work presented descriptions of the described robot's kinematic and dynamic models, as well as preliminary results in analyzing its locomotion using different combinations of commanded joints for the former and a simple feedback controller for the latter. The present article provides further intuition that may help explain the quantitative results that we found from our kinematic analysis, specifically regarding how gaits in different directions may assist in "pulling" the robot to locomote effectively or "pushing" the robot into singularity configurations. We have also added a more rigorous analysis of the dynamic model by using a "harmonic balance" method to describe periodic solutions of passive joints. Finally, a significant contribution of this article is the experimental validation of our findings on a real multi-link robot.

## 2. Prior work

An early experimental implementation of the wheeled snake robot shown in Figure 1 was the Active Cord Mechanism Model 3 of Hirose (1993), for which the author presented a heuristically derived position controller. Krishnaprasad and Tsakiris (1994) introduced the notion of non-holonomic kinematic chains, formalizing the snake robot's configuration as a principal bundle in which periodic "internal" joint angle trajectories are lifted via a connection to a geometric phase, or displacement, in the "external" position variables. Ostrowski and Burdick (1996) considered specific gaits for a three-link robot, including those that induce "serpentine" and rotation motion.

The three-link robot is the simplest instance of this mechanism that can locomote, and as such it has received considerable attention from researchers such as Ostrowski (1999) and Shamma et al. (2007) treating it as a *kinematic* system, so named because its three constraints eliminate the need to consider second-order dynamics when modeling its locomotion. This allows for the treatment of the system's

locomotion, and subsequent motion planning, as a result of geometric phase (Bloch et al., 2003; Bullo and Lynch, 2001; Kelly and Murray, 1995; Mukherjee and Anderson, 1993; Murray and Sastry, 1993; Ostrowski and Burdick, 1998; Ostrowski et al., 2000; Shapere and Wilczek, 1989). The mathematical structure of this system also lends itself to visualization and design tools, detailed by Hatton and Choset (2011).

A branch of later work focused on developing feedback controllers for certain gaits and relaxed mechanism designs. Prautsch and Mita (1999) and Prautsch et al. (2000) proposed a position controller with all joints required to be actuated and centered about zero, but the gaits could not be applied to a three-link robot owing to singularities. Matsuno and Mogi (2000), Matsuno and Suenaga (2003), and Matsuno and Sato (2005) developed the idea of a "redundancy controllable" system and associated position controllers using both kinematic and dynamic models. This allowed for a greater variety of gaits and locomotion, but required the removal of non-holonomic constraints along the mechanism where control was to be imposed. Their controllers were able to actively steer away from singular configurations.

For a general  $m$ -link system, singular states may entail the loss of a controlled degree of freedom (DOF), so motion plans often actively avoid the straight or arc configurations in snake robots, as done by Ye et al. (2004) and Matsuno and Sato (2005). A full analysis of the conditions for singular configurations in a  $m$ -link robot was done by Tanaka and Tanaka (2016) and recently by Yona and Or (2019), the latter of which considered friction bounds and stick-slip transitions of skidding in their models. In preceding work on the three-link robot (Dear et al., 2016a,b, 2017), we showed how to appropriately model the transitions between normal and singular system operation under a hybrid model, and we described how this may be achieved in a physical system with external forcing, as well as its novel locomotive capabilities. We also showed that attaching a spring to the passive joint can replicate this behavior without relying on external forces, allowing for dynamic motions.

## 3. Kinematic model

We now consider a kinematic model for a general  $m$ -link robot. Actuation will be limited to two joints at a time; any more than that will lead to an overconstrained system, as we show in the following. We describe how singularities and stationary joint behaviors arise owing to relative phase relationships among the joints, and then show how the robot is able to execute more natural "slithering" gaits that lead to overall locomotion.

The system shown in Figure 1 is a visual representation of a five-link non-holonomic snake robot. An  $m$ -link robot simply has the requisite number of links appended or removed as necessary. Each link has an identical length  $R$

and a non-holonomic constraint at the link center. The actuation of the joints and subsequent rotation of the links induce locomotion of the overall system, governed by the velocity constraints.

The robot's configuration is denoted  $q \in Q$ , where the configuration space  $Q$  is a product of two distinct subspaces,  $G \times B$ . For this system,  $g = (x, y, \theta)^T \in G = SE(2)$  are Lie group variables specifying the position and orientation of the proximal link, and the joint angles  $b = (\alpha_1, \dots, \alpha_{m-1})^T \in B = \mathbb{T}^{m-1}$  describe the links' relative orientations to one another. In this article, links are numbered 1 (proximal) through  $m$  (distal) and joints 1 through  $m - 1$ , with joint  $i$  connecting links  $i$  and  $i + 1$ .

The kinematics of the system are described by the set of non-holonomic constraints on the wheels, which prohibit motion perpendicular to each of the links' longitudinal directions. They can be written as  $m$  equations of the form

$$-\dot{x}_i \sin \theta_i + \dot{y}_i \cos \theta_i = 0 \quad (1)$$

where  $(\dot{x}_i, \dot{y}_i)$  is the velocity and  $\theta_i$  is the inertial orientation of the  $i$ th link. These quantities can be computed recursively in order to express them as functions of  $q$ . Starting with the proximal link, we have that  $(x_1, y_1, \theta_1) = (x, y, \theta)$ ; for  $i = 2, \dots, m$ ,

$$\begin{aligned} \theta_i &= \theta_{i-1} + \alpha_{i-1} \\ x_i &= x_{i-1} + \frac{R}{2}(\cos \theta_{i-1} + \cos \theta_i) \\ y_i &= y_{i-1} + \frac{R}{2}(\sin \theta_{i-1} + \sin \theta_i) \end{aligned} \quad (2)$$

The constraint equations are symmetric (Kelly and Murray, 1995) with respect to the group part  $G$  of the configuration, because the kinematics do not explicitly depend on the system's position or orientation in space. The space  $Q$  can thus be described formally as a *principal fiber bundle* (Abraham et al., 1978; Marsden et al., 1990) with the fibers  $G$  over the base manifold  $B$ . In such a structure, trajectories specified only in the base (or otherwise known as shape) space  $B$  can be mapped to trajectories in the position space  $G$ .

In order to find such a mapping, we can rewrite the constraints in a reduced Pfaffian form as

$$\omega_\xi(b)\xi + \omega_b(b)\dot{b} = 0 \quad (3)$$

where  $\omega_\xi \in \mathbb{R}^{m \times 3}$ ,  $\omega_b \in \mathbb{R}^{m \times (m-1)}$ , and  $\xi = (\xi_x, \xi_y, \xi_\theta)^T \in \mathfrak{se}(2)$  are the fiber velocities of the system expressed in a frame attached to the proximal link, as shown in Figure 1. These "body velocities" can be viewed as the inertial group velocities  $\dot{g} = (\dot{x}, \dot{y}, \dot{\theta})$  transformed to the tangent space at the identity element  $e$  of  $G$ . Note while  $\dot{g}$  and  $\xi$  are fundamentally different quantities living in different spaces, they play a similar role in describing the velocity of the system, but relative to different frames. There is a one-to-one mapping between them given the system's orientation  $\theta$ , and we assume in this work that one can

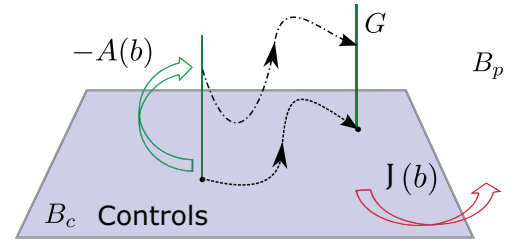


**Fig. 2.** A principal fiber bundle with a separate space of base variables that evolve according to a set of kinematics given by  $J$ . The original connection  $-A$  lifts complete base trajectories to the fibers.

freely transform back and forth as needed. This mapping is formally expressed as  $\xi = (T_e L_g)^{-1} \dot{g}$ , where  $T_e L_g$  is the *lifted left action* given by

$$T_e L_g = \begin{pmatrix} \cos \theta & -\sin \theta & 0 \\ \sin \theta & \cos \theta & 0 \\ 0 & 0 & 1 \end{pmatrix}$$

Typically, one assumes that input commands are sent to the joint variables  $b$ . For a three-link robot ( $m - 1 = 2$ ), the number of constraints coincides exactly with the dimension of the fiber. By specifying trajectories in both joint (shape) variables, fiber trajectories are then determined exactly by the constraint equations. For a robot with greater than three links, or  $m > 3$ , each additional joint DOF is added along with a new constraint on the overall system's motion, preventing the system from gaining an additional free controlled input. We can therefore arbitrarily control at most two joint DOFs if all the constraints are to hold.

In this section, we consider systems with exactly two input DOFs at any given time, denoted as  $b_c = (\alpha_i, \alpha_j)^T$ . The rest of the joint variables are denoted  $b_p$  and evolve kinematically according to the constraints. Equation (3) can then be rewritten as

$$\begin{aligned} \xi &= -A(b)\dot{b}_c \\ \dot{b}_p &= J(b)\dot{b}_c \end{aligned} \quad (4)$$

Here we explicitly separate the mappings from  $\dot{b}_c$  to  $\xi$  and  $\dot{b}_c$  to  $\dot{b}_p$ ;  $-A(b) \in \mathbb{R}^{3 \times 2}$  is the *local connection form*, a mapping that lifts trajectories in the base to the fiber, whereas  $J(b) \in \mathbb{R}^{(m-3) \times 2}$  is a Jacobian-like relationship (though not a connection) between the commanded joint velocities  $\dot{b}_c$  and the passive ones  $\dot{b}_p$ . This dual structure can be visualized as shown in Figure 2. Equation (4) can be further simplified into a chained form, which will aid us in analysis of the special cases of two adjacent commanded and two non-adjacent commanded joints in the following sections.

**Proposition 1.** Suppose that  $b_c = (\alpha_i, \alpha_j)^T$  where  $i < j$ . Then

$$\dot{\alpha}_k = \begin{cases} f_k(\alpha_k, \alpha_{k+1}, \dots, \alpha_{j-1}, \alpha_j) \dot{b}_c, & k < i \\ f_k(\alpha_i, \alpha_{i+1}, \dots, \alpha_{k-1}, \alpha_k) \dot{b}_c, & k > j \\ f_k(\alpha_i, \alpha_{i+1}, \dots, \alpha_{j-1}, \alpha_j) \dot{b}_c, & i < k < j \end{cases} \quad (5)$$

Furthermore, the kinematics of the proximal link can be written as

$$\xi = -A(\alpha_1, \alpha_2, \dots, \alpha_{j-1}, \alpha_j) \dot{b}_c \quad (6)$$

In other words, the kinematics of any joint only depend on the joint configurations between itself and the most distal controlled joint in both directions.

*Proof.* Owing to the recursive nature of how the constraint equations are defined, one can algebraically show that the constraint matrices in Equation (3) have the forms

$$\omega_\xi = \begin{pmatrix} 0 & 1 & 0 \\ -\sin \alpha_1 & \cos \alpha_1 & f(\alpha_1) \\ -\sin(\alpha_1 + \alpha_2) & \cos(\alpha_1 + \alpha_2) & f_{1,2} \\ \vdots & \vdots & \vdots \\ -\sin\left(\sum_{l=1}^{m-1} \alpha_l\right) & \cos\left(\sum_{l=1}^{m-1} \alpha_l\right) & f_{1,m-1} \end{pmatrix}$$

$$\omega_b = \begin{pmatrix} 0 & 0 & 0 & \dots & 0 \\ R/2 & 0 & 0 & \dots & 0 \\ f(\alpha_2) & R/2 & 0 & \dots & 0 \\ f_{2,3} & f(\alpha_3) & R/2 & \ddots & \vdots \\ \vdots & \vdots & \ddots & \ddots & 0 \\ f_{2,m-1} & f_{3,m-1} & & f(\alpha_{m-1}) & R/2 \end{pmatrix}$$

where  $f_{i,j} = f(\alpha_i, \alpha_{i+1}, \dots, \alpha_j)$ .

The  $k$ th row of each matrix, which corresponds to the  $k$ th constraint equation, only has dependencies on the joint angles  $\alpha_1, \dots, \alpha_{k-1}$ . Furthermore, since all  $m$  constraints are independent, the first  $j+1$  rows of both matrices yield  $j+1$  independent equations. These equations are linear in the body velocities ( $\xi_x, \xi_y, \xi_\theta$ ) as well as the joint velocities ( $\dot{\alpha}_1, \dots, \dot{\alpha}_j$ ). Given that we have command over the two joints  $\alpha_i$  and  $\alpha_j$ , this leaves us with  $j+1$  unknown velocity quantities (three fibers plus  $j-2$  joints), which can be linearly solved.

We now have a solution for the joint velocities  $\dot{\alpha}_k$  with  $k < j$ . The kinematic maps for these solutions have dependencies from  $\alpha_1$  to  $\alpha_j$  only, because no equations past the first  $j+1$  rows of the constraint matrices are used. This thus proves Equation (6). We can now solve for the joint velocities  $k > j$  by successively using each of the constraint equations in order starting from row  $j+2$  of the constraint matrices. Each equation has dependencies up to  $\alpha_k$  and introduces one unknown joint velocity  $\dot{\alpha}_k$ , which can be solved since the previous velocities are already known.

We now know that the kinematics must be of the form

$$\dot{\alpha}_k = \begin{cases} f_k(\alpha_1, \dots, \alpha_j) \dot{b}_c, & k < j \\ f_k(\alpha_1, \dots, \alpha_k) \dot{b}_c, & k > j \end{cases} \quad (7)$$

A symmetry argument can be applied. Our choices of the proximal link and the joint  $\alpha_1$  are arbitrarily defined, with the physical kinematics of the system being unchanged if we had instead chosen to start  $\alpha_1$  from the most distal link. Therefore, by defining the constraints relative to that link and going through the same procedure as above, we would obtain (in the original coordinates)

$$\dot{\alpha}_k = \begin{cases} f_k(\alpha_k, \dots, \alpha_{m-1}) \dot{b}_c, & k < i \\ f_k(\alpha_i, \dots, \alpha_{m-1}) \dot{b}_c, & k > i \end{cases} \quad (8)$$

In order for both Equations (7) and (8) to hold simultaneously, the dependencies must only occur in their intersection. In other words, the function  $f_k$  has a dependency on an arbitrary joint  $\alpha_l$  only if this is true in both equations. Equation (5) can then be proved by applying this observation to each joint velocity in turn.  $\square$

### 3.1. Adjacent commanded joints

*3.1.1. Three-link robot.* In considering the overall locomotion of the multi-link snake robot, we first take the case in which the two commanded joints are adjacent to each other, i.e.,  $b_c = (\alpha_i, \alpha_{i+1})^T$ . As each successive joint's kinematics depend only on that of the joints before it, the evolution of the passive joint variables increases in complexity as they get farther away from  $\alpha_i$  or  $\alpha_{i+1}$ . We first review previous work regarding the simplest relevant configuration for this case, the three-link robot. For this system, one assumes command of both joint variables  $\alpha_1$  and  $\alpha_2$ ; there are no remaining passive joints. Then the kinematic mapping for  $\xi$  can be written as

$$\xi = \frac{1}{D} \begin{pmatrix} \cos \alpha_1 + \cos(\alpha_1 - \alpha_2) & 1 + \cos \alpha_1 \\ 0 & 0 \\ \frac{2}{R}(\sin \alpha_1 + \sin(\alpha_1 - \alpha_2)) & \frac{2}{R} \sin \alpha_1 \end{pmatrix} \begin{pmatrix} \dot{\alpha}_1 \\ \dot{\alpha}_2 \end{pmatrix} \quad (9)$$

where  $D = \frac{2}{R}(-\sin \alpha_1 - \sin(\alpha_1 - \alpha_2) + \sin \alpha_2)$ . The second row, corresponding to  $\xi_y$ , is zero since this corresponds to the direction prohibited by the wheel of the proximal link.

We can also consider the general  $m$ -link robot. Note that Equation (9) describes the fiber motion of an  $m$ -link robot and is a special form of Equation (6). If either  $\alpha_1$  or  $\alpha_2$  is unactuated when  $m > 3$ , we can use Equation (5) to first solve for the passive joint trajectories in terms of the controlled ones, and then apply Equation (9) to find the overall fiber motion.

The quantity  $\frac{1}{D}$  is not defined when  $\alpha_1 = \alpha_2$ , which corresponds to a singular configuration for the system. Such a configuration corresponds to the links of the robot lying along the same arc, as shown in Figure 3. We no longer have three independent constraints in our kinematic model, and having only two of them is insufficient to prescribe the three fiber DOFs when moving the joint angles into or from this configuration. For general operation of a

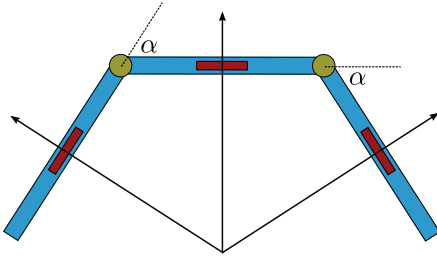


**Fig. 3.** The three-link snake robot in a singular configuration. Its links lie along the same arc, and the directions associated with the non-holonomic constraints intersect at the same point.

multi-link robot with two commanded joint inputs, we will also prefer gaits that avoid this and other singular configurations.

The structure of the connection form in Equation (9) can be visualized in order to understand the response of  $\xi$  to input trajectories, according to Hatton and Choset (2011). We can first integrate each row of Equation (9) over time to obtain a measure of displacement corresponding to the body frame directions. In the world frame, this measure provides the exact rotational displacement, i.e.,  $\theta = \xi_\theta$  for the third row, and an approximation of the translational component for the first two rows. This “body velocity integral” is expressed as

$$\zeta(t) = - \int_0^t A(b(\tau)) \dot{b}(\tau) d\tau \quad (10)$$

If our input trajectories are periodic, we can convert the body velocity integral over time into one over the trajectory  $\psi : [0, T] \rightarrow B$  in the joint space, since the kinematics are independent of input pacing. Stokes’ theorem can then be applied to perform a second transformation into an area integral over  $\beta$ , the region of the joint space enclosed by  $\psi$ :

$$\zeta_\psi = - \int_\psi A(b) db = - \int_\beta dA(b) \quad (11)$$

The integrand in the integral on the right-hand side is the exterior derivative of  $A$  and is computed as the curl of  $A$  in two dimensions. For example, the connection exterior derivative of Equation (9) has three components, one for each row  $i$  given by

$$dA_i(b) = \frac{\partial A_{i,2}}{\partial \alpha_1} - \frac{\partial A_{i,1}}{\partial \alpha_2}$$

where  $A_{i,j}$  is the element corresponding to the  $i$ th row and  $j$ th column of  $A$ .

The magnitudes of the connection exterior derivative over the joint space are depicted in Figure 4,<sup>1</sup> along with a gait trajectory shown as a closed curve on the surfaces. The area integral over the enclosed region is the geometric phase, a measure of the expected displacement in the body  $x$  and  $\theta$  directions (the body  $y$  plot is not shown because it

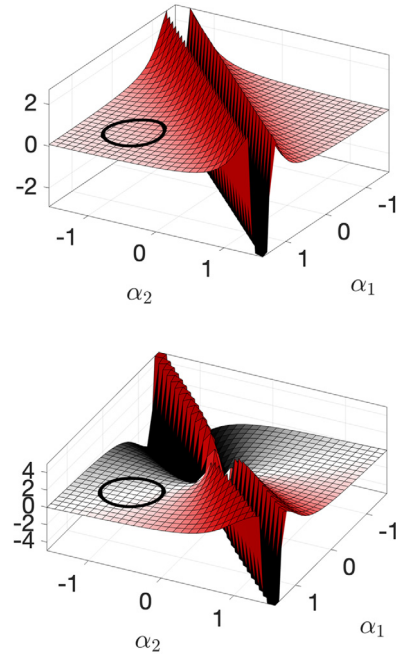


**Fig. 4.** Visualizations of the  $x$  and  $\theta$  components of the connection exterior derivative for the three-link snake robot.

is zero everywhere). The  $x$  plot is positive everywhere, meaning that any closed loop will lead to net displacement along the  $\xi_x$  direction. In particular, a trajectory that advances in a *counter-clockwise* direction over time in joint space will yield positive body- $x$  displacement, because that corresponds to a positive area integral; negative body- $x$  displacement is achieved with a *clockwise* trajectory. The  $\theta$  plot is anti-symmetric about  $\alpha_1 = -\alpha_2$ , meaning that gaits symmetric about this line will yield zero net reorientation while simultaneously moving the robot forward. Note that the magnitudes in both plots become unbounded closer to the singular configurations  $\alpha_1 = \alpha_2$ .

**3.1.2. Stationary passive joint.** Our analysis for a three-link robot helps us understand the types of gaits that would emerge for a robot with more than three links, where the commanded joints are  $\alpha_i$  and  $\alpha_{i+1}$  and those on either side of them are passive. In general, the kinematics of a joint  $\alpha_{i+2}$  (or  $\alpha_{i-1}$  by symmetry) in response to two adjacent joints  $\alpha_i$  and  $\alpha_{i+1}$  are given by

$$\begin{aligned} \dot{\alpha}_{i+2} &= \frac{\cos(\frac{1}{2}\alpha_{i+2})}{\sin(\frac{1}{2}(\alpha_i - \alpha_{i+1}))} \\ &\left( \frac{\sin(\frac{1}{2}(\alpha_{i+1} - \alpha_{i+2}))}{\cos(\frac{1}{2}\alpha_i)} \dot{\alpha}_i - \frac{\sin(\frac{1}{2}(\alpha_i - 2\alpha_{i+1} + \alpha_{i+2}))}{\cos(\frac{1}{2}\alpha_{i+1})} \dot{\alpha}_{i+1} \right) \\ &\triangleq A_{i+2} \begin{bmatrix} \dot{\alpha}_i \\ \dot{\alpha}_{i+1} \end{bmatrix} \end{aligned} \quad (12)$$

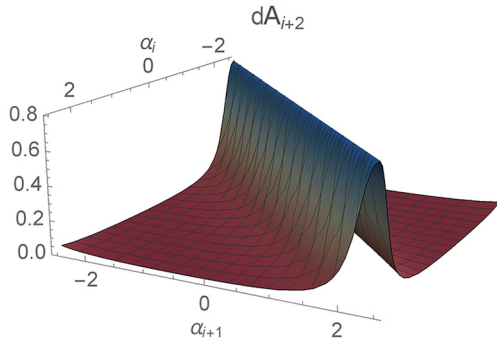


**Fig. 5.** The Jacobian exterior derivative of  $A_{i+2}$  when  $\alpha_{i+2}$  is close to but less than  $\pi$ .

An immediate observation, other than the same singularity of  $\alpha_i = \alpha_{i+1}$  of a three-link robot, is that  $\alpha_{i+2} = \pm\pi$  are equilibria, as  $\dot{\alpha}_{i+2}$  is zero at these configurations. This corresponds to the passive joint rotating all the way around such that link  $i+2$  coincides with link  $i+1$ , normally an undesirable behavior. We must therefore investigate the stability of the equilibrium at  $\pi$ ; in order to not remain stationary,  $\dot{\alpha}_{i+2}$  should be negative if  $\alpha_{i+2} = \pi - \epsilon$  and positive if  $\alpha_{i+2} = -\pi + \epsilon$ , where  $\epsilon$  is a small positive number. It can be shown that Equation (12) is simply negated between the two cases, so any solution that causes one equilibrium to be unstable will also be sufficient for the other.

In the same way that we visualize the exterior derivative of the connection form from Equation (9), we can also visualize the exterior derivative of  $A_{i+2}$  of Equation (12). By plotting the magnitude of the curl of  $A_{i+2}$ , we can see whether a given combination of  $\alpha_i$  and  $\alpha_{i+1}$  pushes  $\alpha_{i+2}$  toward or away from  $\pm\pi$ . This is shown as the surface in Figure 5 for  $\alpha_{i+2} = \pi - \epsilon$ , where  $\epsilon$  is a small positive number (again, this would be negated for  $\alpha_{i+2} = -\pi + \epsilon$ ).

While the absolute magnitudes are not important, it is positive everywhere, analogous to the  $x$  exterior derivative plot. Any closed loop that is traversed in a *counterclockwise* direction on the surface will yield a positive net area, pushing  $\alpha_{i+2}$  toward  $\pi$ . Physically, the robot is attempting to move backward relative to the positions of its actuated joints, forcing the robot’s tail to fold into the body. In order to obtain the opposite result, we must have gaits corresponding to *clockwise* loops, which integrate to negative values and push  $\alpha_{i+2}$  away from  $\pi$ . In the  $\alpha_i$ - $\alpha_{i+1}$  space, clockwise loops are those in which  $\alpha_{i+1}$  leads  $\alpha_i$ ; i.e., their phase difference is between 0 and  $\pi$ . In contrast to the prior scenario, here the robot’s tail is being dragged along while it moves forward, so the tail will not fold into the body. This is reminiscent of the truck and passive-trailer problem, which is relatively easy to control if the truck “pulls” its trailer forward but becomes unstable if the truck “pushes” its trailer backward, as shown by authors such as Altafini et al. (2001).

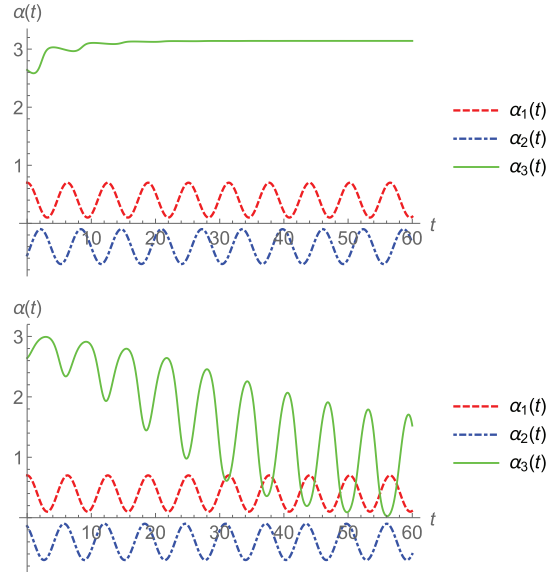


**Fig. 6.** Trajectories of commanded inputs  $\alpha_1$  and  $\alpha_2$ , and the passive response  $\alpha_3$ . The inputs’ relative phase determines the convergent behavior of  $\alpha_3$ ;  $\alpha_3$  moves toward a stationary configuration when  $\alpha_1$  leads  $\alpha_2$ , while  $\alpha_3$  oscillates when the opposite is true.

Figure 6 shows two simulations for a four-link robot verifying our conclusion. The commanded inputs (dashed lines) are  $\alpha_1 = 0.3 \cos(t) + 0.4$  and  $\alpha_2 = 0.3 \cos(t + \phi) - 0.4$ , where  $\phi = \frac{4\pi}{3}$  in the first simulation, causing  $\alpha_2$  to lag  $\alpha_1$ , and  $\phi = \frac{\pi}{6}$  in the second, so that  $\alpha_2$  leads  $\alpha_1$ . In the former case, the passive response of  $\alpha_3$  (solid line) converges toward  $\pi$  and stays there throughout the trajectory. The opposite is true in the second plot, even though  $\alpha_3$  starts out very close to  $\pi$  and is even initially drawn to it before the end of the first gait cycle.

**3.1.3. Oscillating passive joints.** Assuming that  $\alpha_i$  and  $\alpha_{i+1}$  are prescribed so that the adjacent passive joint  $\alpha_{i+2}$  does not remain stationary,  $\alpha_{i+2}$  will have a steady-state oscillatory response. Our analysis in the previous section strongly suggests that the relative phase difference between the two actuated joints, assuming sinusoidal trajectories, is a determining factor for the robot’s resultant behavior. From the second plot of Figure 6, we see that  $\alpha_3$  converges toward a trajectory that is nearly completely out of phase with  $\alpha_2$ . This observation holds exactly if  $\alpha_3$  happens to intersect  $\alpha_2$  anywhere along its steady-state trajectory, i.e.,  $\alpha_3(\tau) = \alpha_2(\tau)$  for some time  $\tau$ , as Equation (12) reduces to  $\dot{\alpha}_3(\tau) = -\dot{\alpha}_2(\tau)$ . This means that the two trajectories are out of phase with each other.

Based on simulations and a linearization analysis of Equation (12), we make the following observations about the oscillatory response of  $\alpha_{i+2}$  owing to sinusoidal inputs with the same frequency but possibly different phase. We assume that  $\phi$  is chosen so that  $\alpha_{i+2}$  does not end up stationary. We also assume that the magnitudes and offsets are

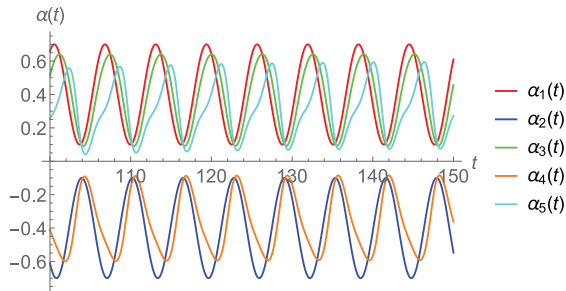


**Fig. 7.** Trajectories of commanded inputs  $\alpha_1$  and  $\alpha_2$ , and the passive response of joint angles  $\alpha_3$ ,  $\alpha_4$ , and  $\alpha_5$ .

such that the  $\alpha_i$  and  $\alpha_{i+1}$  trajectories do not intersect, ensuring that the robot avoids singular configurations.

1. The magnitude of  $\alpha_{i+2}$  depends on  $\phi$ . When the commanded joints are in phase,  $\alpha_{i+2}$  has a magnitude close to the sum of the magnitudes of  $\alpha_i$  and  $\alpha_{i+1}$  (i.e., they are superimposed). Otherwise, it is about the same magnitude as the smaller of  $\alpha_i$  and  $\alpha_{i+1}$ .
2.  $\alpha_{i+2}$  operates nearly out of phase to  $\alpha_{i+1}$ , regardless of the original phase  $\phi$ .
3. The offset of  $\alpha_{i+2}$  is closer to that of  $\alpha_i$  than  $\alpha_{i+1}$ , so that the proximal robot configuration tends toward a “zig-zag” shape.

These observations can be carried over to passive joints beyond  $\alpha_{i+2}$ . Although the velocity description of an arbitrary joint  $\alpha_j$  becomes increasingly complex and depends on all of the joints preceding it, the principal response of  $\alpha_j$  is to move “opposite” to  $\alpha_{j-1}$ . Thus, a natural mode of locomotion is that each successive joint trajectory alternates between the two forms set by the commanded joints, with slight decays in magnitude, phase, and offset going down the links. Figure 7 depicts the trajectories of three passive joints in response to arbitrary inputs to  $\alpha_1$  and  $\alpha_2$ . The first passive joint  $\alpha_3$  follows a trajectory close to  $\alpha_1$ , while leading  $\alpha_2$  by about the same phase that  $\alpha_2$  leads  $\alpha_1$ . The same statements can be made for  $\alpha_4$  and  $\alpha_5$ , each relative to the preceding joints. Note that the magnitudes and sinusoidal form increasingly decay as we move down the chain, because each passive joint does not perfectly replicate the opposite gait of the preceding one. A snapshot of the robot’s configuration during these joint trajectories is shown in Figure 8. This dynamic zig-zag shape is maintained throughout the locomotion of the robot.

We can make several statements about the overall locomotion of the robot as a result of different joint interactions. First, because the kinematics are of a chained form, the presence of links and passive joints beyond the standard three-link case does not change the locomotion of the proximal link as long as  $\alpha_1$  and  $\alpha_2$  are the commanded joints. Second, commanding successive joints in the interior of the robot, i.e., joints that are neither  $\alpha_1$  nor  $\alpha_{m-1}$ , is to be avoided in order to prevent an adjacent passive joint from

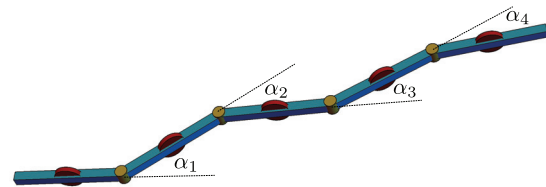


**Fig. 8.** Depiction of the natural “zig-zag” configuration achieved by the passive joints ( $\alpha_3$  and  $\alpha_4$ ) of a five-link robot.

becoming stationary. If  $\alpha_i$  leads  $\alpha_{i+1}$ ,  $\alpha_{i+2}$  will lock, as per our earlier conclusion; if the opposite is true,  $\alpha_{i+1}$  leads  $\alpha_i$  and so  $\alpha_{i-1}$  will lock. Since it is inevitable that a passive joint on either side of the two controlled ones will become stuck, we can conclude that the two actuated joints must be located at either the proximal or distal end of the robot to avoid any of the joints becoming stationary.

### 3.2. Non-adjacent commanded joints

The analysis of the previous subsection can be extended to situations in which the commanded subset of joints is not located adjacently. Previously, we found that to avoid joint convergence to stationary configurations, the two adjacent commanded joints must be located at either the front end ( $\alpha_1, \alpha_2$ ) or the back end ( $\alpha_{m-1}, \alpha_m$ ), making the robot’s fiber locomotion equivalent to that of a three-link robot. In other words, the kinematic model asserts that adding an arbitrary number of passive joints and links to a three-link robot with the original joints actuated does not change how the robot moves. Here we show that non-adjacent commanded joints can potentially avoid becoming stationary and allow for commanded joints away from the ends of the robot. The kinematics of a passive joint  $\alpha_i$  between two commanded ones  $\alpha_{i-1}$  and  $\alpha_{i+1}$  are given by

$$\dot{\alpha}_i = \frac{\cos(\frac{1}{2}\alpha_i)}{\sin(\frac{1}{2}(\alpha_{i-1} - 2\alpha_i + \alpha_{i+1}))} \left( \frac{\sin(\frac{1}{2}(\alpha_i - \alpha_{i+1}))}{\cos(\frac{1}{2}\alpha_{i-1})} \dot{\alpha}_{i-1} + \frac{\sin(\frac{1}{2}(\alpha_i - \alpha_{i-1}))}{\cos(\frac{1}{2}\alpha_{i+1})} \dot{\alpha}_{i+1} \right) \triangleq A_i \begin{bmatrix} \dot{\alpha}_{i-1} \\ \dot{\alpha}_{i+1} \end{bmatrix} \quad (13)$$

The form of this equation shares some similarities with Equation (12). However, in addition to again having undesired equilibria at  $\alpha_i = \pm\pi$ , it is now also possible for the robot to passively find itself in a singular configuration if the sine term in the denominator goes to zero. Note that the singularities here are of a different nature from those of Equation (12), which correspond to the two adjacent joints having equal values. In that case, the inputs can directly be

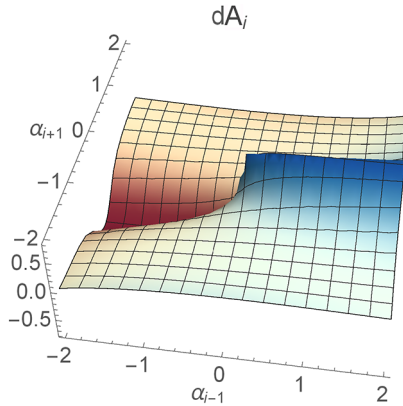


**Fig. 9.** The exterior derivative of the Jacobian  $A_i$  close to a singularity, for  $\alpha_i \approx \frac{1}{2}(\alpha_{i-1} + \alpha_{i+1})$ .

chosen to avoid those configurations. Here, in Equation (13) a singular configuration is one in which  $\alpha_i = \frac{1}{2}(\alpha_{i-1} + \alpha_{i+1})$ , where the critical difference from the previous example is that the left-hand side is a quantity that we do not control directly.

Valid gaits are those that would push  $\alpha_i$  away from the average of  $\alpha_{i-1}$  and  $\alpha_{i+1}$  when it is near the aforementioned value. As previously, we can visualize the exterior derivative of the Jacobian  $A_i$  of Equation (13), shown in Figure 9 for  $\alpha_i = \frac{1}{2}(\alpha_{i-1} + \alpha_{i+1}) - \epsilon$ , where  $\epsilon$  is again a small positive number. As we would like  $\alpha_i$  to decrease, we seek a loop that encloses a negative net area. From inspection, we have that a loop lying mostly above the  $\alpha_{i-1} = \alpha_{i+1}$  line (upper left-hand side of the plot) should run counterclockwise, and vice versa for a gait below that line. Unlike in Figure 5, the surface of Figure 9 is not sign-definite; the phasing of the gait is no longer sufficient to determine the sign of the enclosed area, and integration is required to determine the net area for gaits in which the averages of  $\alpha_{i-1}(t)$  and  $\alpha_{i+1}(t)$  are close in value. A rule of thumb is that the joint trajectory whose average value is smaller (a lower offset) should lead the other.

Figure 10 shows the joint trajectories for a four-link robot, in which  $\alpha_1$  and  $\alpha_3$  are controlled and  $\alpha_2$  is passive. In both simulations,  $\alpha_1(t) = 0.3 \cos(t) + 0.4$  and  $\alpha_3(t) = 0.3 \cos(t + \phi) + 0.5$ , with  $\phi = -\frac{\pi}{3}$  in the first and  $\phi = \frac{\pi}{3}$  in the second. In the first case, the  $\alpha_1$  trajectory, which has a smaller average value, leads  $\alpha_3$ , so that  $\alpha_2$  is not attracted into the singular configuration and instead settles into an oscillatory trajectory with an offset opposite the trajectories on either side of it. This is consistent with what we found in Figure 7, in which the roles of  $\alpha_2$  and  $\alpha_3$  are switched but the trajectories remain similar. However, when  $\alpha_3$  is made to lead  $\alpha_1$  in the second plot of Figure 10, we have that  $\alpha_2$  is attracted to the value of  $\frac{1}{2}(\alpha_1 + \alpha_3)$  at  $t = 2.9$ , at which point the kinematic model produces a singularity.

If we have a valid gait trajectory that can avoid singular configurations, the general characterizations of oscillating passive joint behaviors in the previous subsection can be

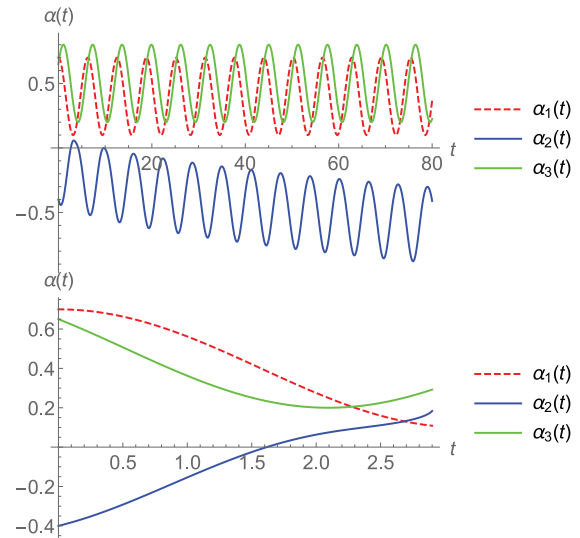


**Fig. 10.** Trajectories of commanded inputs  $\alpha_1$  and  $\alpha_3$ , and the passive response  $\alpha_2$ . The inputs' relative phase determines the convergent behavior of  $\alpha_2$ ; the top simulation shows  $\alpha_2$  oscillating in a stable manner, whereas the bottom one has  $\alpha_2$  converging toward a singularity, preventing the simulation from running forward.

applied here to inform a rudimentary feedback controller for locomotion. For example, suppose that we have a four-link robot in which the two outer joints  $\alpha_1$  and  $\alpha_3$  are commanded and the inner joint  $\alpha_2$  is passive. As we know that locomotion of the proximal link can be found from  $\alpha_1$  and  $\alpha_2$  only (Equation (9)), we can achieve desired  $\alpha_1$  and  $\alpha_2$  trajectories by prescribing  $\alpha_1$  and then “shaping”  $\alpha_2$  using  $\alpha_3$ . The qualitative aspects of a shaping controller are as follows.

1. The phase of  $\alpha_2$  is approximately the average of the phases of  $\alpha_1$  and  $\alpha_3$ , plus an additional  $\pi$  offset.
2. The offset of  $\alpha_2$  depends on its initial value, but can be changed by shifting the offset or magnitude of  $\alpha_3$  relative to  $\alpha_1$  in the opposite direction.
3. The magnitude of  $\alpha_2$  is determined by its phase with respect to the commanded joints. A larger magnitude can be achieved by scaling  $\alpha_3$  proportionally when the trajectories are close to in phase.

Given a fixed trajectory  $\alpha_1$  and a desired trajectory for  $\alpha_2$ , we can use the above guidelines to impose proportional or more complex feedback controllers on the parameters of  $\alpha_3$ . However, these controllers do not necessarily always converge, because the ability to shape the passive joint is rigidly limited by the possibility of hitting singular configurations. For example, the offset of  $\alpha_2$  may not be so close to the other two trajectories that it intersects them, limiting how much control we have over its magnitude. The robustness and convergence of this or an improved controller will be considered in future work.

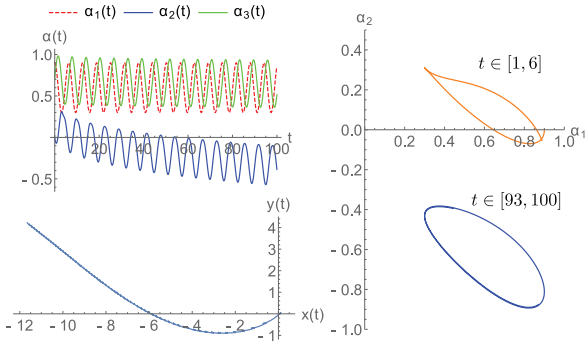


**Fig. 11.** Using  $\alpha_3$  to shape  $\alpha_2$  over time (top left) and achieving a desired trajectory in the  $\alpha_1$ – $\alpha_2$  space (right). Bottom left: The robot's fiber motion.

In the simulation of Figure 11,  $\alpha_1(t)$  follows a prescribed trajectory, but we desire to control  $\alpha_3$  so as to move  $\alpha_2$  farther away from the origin with an offset  $a_d$  and a phase  $\phi_2$ . We use a feedback controller of the form

$$\alpha_3(t) = \alpha_1(t - 2\phi_2) + k_p \left( \frac{1}{2} (\alpha_1(t) - \alpha_2(t)) - a_d \right) \quad (14)$$

where  $k_p$  is the controller gain. As can be seen in the top left plot, the effect of the controller is to shrink  $\alpha_3$  (green) in magnitude and shift it downward over time. In response,  $\alpha_2$  (blue) decreases its offset away from  $\alpha_1$  and  $\alpha_3$ . The right plot shows a sampling of the trajectories in  $\alpha_1$ – $\alpha_2$  space, where they are mostly elliptical loops starting near the  $\alpha_1$  axis (orange) and then eventually moving downward toward the  $\alpha_1 = -\alpha_2$  line (blue). Finally, from the robot's connection derivative plots of Figure 4, we know that these gaits will increase the reorientation of the robot from negative to zero, which is verified by the bottom left plot of the robot's fiber trajectory showing the change in curvature over time. If  $\alpha_2$  is further decreased, then the gaits become closer to the negative regions of  $dA_\theta$  (shown as red in Figure 4), which will cause the robot's trajectory to acquire the opposite curvature.

#### 4. Dynamic model

We have shown that the kinematic model of the  $m$ -link robot is derived solely from the constraints, with each passive joint described by a first-order differential equation depending only on the joint angles between it and the commanded ones. Such a model is useful if exactly two joints are commanded. If only one joint is commanded, then a more general dynamic model is required to determine the interactions among all of the passive joints.

In addition, we have also seen that purely kinematic trajectories can be susceptible to joint locking, as well as singular configurations, such that the robot cannot execute arbitrary trajectories following the two prescribed inputs. We will show in this section that a full dynamic model (with only one commanded input) allows the robot to be

designed or controlled in a way as to avoid joint locking and singularities.

We assume that each link  $i$  has mass  $M_i^l$  and moment of inertia  $J_i$ , in addition to the identical lengths  $R$ . Each joint  $\alpha_i$  is represented as a point mass  $M_i^j$ , for example capturing motor mass, as well as spring constant  $k_i$ , which represents torsional springs on the passive joints; we assume that the resting configurations are all  $\alpha_i = 0$ . Now the Lagrangian of the whole system can be written as

$$L = \frac{1}{2} \sum_{i=1}^m \left( M_i^l ((\dot{x}_i^l)^2 + (\dot{y}_i^l)^2) + J_i \dot{\theta}_i^2 \right) + \frac{1}{2} \sum_{i=1}^{m-1} \left( M_i^j ((\dot{x}_i^j)^2 + (\dot{y}_i^j)^2) - k_i \alpha_i^2 \right) \quad (15)$$

where  $(x_i^l, y_i^l)$  and  $\theta_i$  are the position and orientation of the  $i$ th link defined by Equation (2), and  $(x_i^j, y_i^j)$  is the position of the  $i$ th joint. Following Shamma et al. (2007), if the body velocities  $\xi$  are substituted in for the inertial fiber velocities, then the Lagrangian can be reduced to a form

$$l(b, \xi, \dot{b}) = \frac{1}{2} \begin{bmatrix} \xi^T & \dot{b}^T \end{bmatrix} \tilde{M}(b) \begin{bmatrix} \xi \\ \dot{b} \end{bmatrix} - \frac{1}{2} \sum_{i=1}^{m-1} k_i \alpha_i^2 \quad (16)$$

where  $\tilde{M}(b)$  is a *reduced mass matrix* with dependencies on the system parameters and joint angles only.

The second-order Euler–Lagrange equations of motion can then be derived, giving us three equations

$$\frac{d}{dt} \left( \frac{\partial l}{\partial \xi_{\{x,y,\theta\}}} \right) - \text{ad}_\xi^* \frac{\partial l}{\partial \xi_{\{x,y,\theta\}}} = \lambda(t) \omega_{\xi, \{x,y,\theta\}} \quad (17)$$

and  $m - 1$  equations

$$\frac{d}{dt} \left( \frac{\partial l}{\partial \dot{\alpha}_i} \right) - \frac{\partial l}{\partial \alpha_i} = \lambda(t) \omega_{b,i} - d_i \dot{\alpha}_i \quad (18)$$

Here,  $\omega_{\xi, \{x,y,\theta\}}$  and  $\omega_{b,i}$  are the indicated columns of the constraint matrices in Equation (3), and  $\lambda(t) = (\lambda_1(t), \dots, \lambda_m(t))$  is a horizontal vector of Lagrange multipliers corresponding to each of the constraints. The adjoint term in Equation (17) corresponds to the collection of terms that results when taking partial derivatives of the reduced Lagrangian and applying the chain rule to account for the change of coordinates from  $\dot{g}$  to  $\xi$  (see Bloch et al. (2003) for a full derivation). Simple viscous dissipation terms  $d_i \dot{\alpha}_i$  are appended to Equation (18) to ensure stability, where  $d_i$  are damping constants. Along with the constraint equations themselves, Equations (17) and (18) can be integrated in order to find the dynamic solutions of the robot.

The dynamical equations can be further reduced to the space of the joint variables by solving Equations (17) and (18) as a linear system in the Lagrange multipliers. Note that we can replace all occurrences of the body velocities  $\xi$  and their derivatives with the base variables, because the

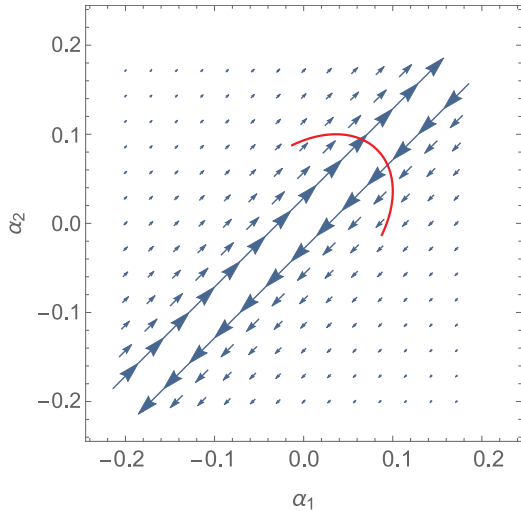


**Fig. 12.** A joint trajectory of a three-link robot overlaid on the  $\xi_x$  vector field component of the connection. Because the trajectory satisfies  $\dot{\alpha}_1 = -\dot{\alpha}_2$ , it is able to pass through the  $\alpha_1 = \alpha_2$  singular configuration without violating the constraints.

original kinematics of the robot (Equation (9)) still hold. This results in a system of  $m + 2$  equations in the base variables  $b$  and their first- and second-order time derivatives, in addition to the Lagrange multipliers. The multiplier variables  $\lambda(t)$  can be further eliminated when combining this system with the time derivative of the three constraint equations (Equation (3)), giving us a system in only  $b$  as

$$\tilde{M}_b(b)\ddot{b} + \tilde{C}(b, \dot{b}) + \tilde{K}(b) = 0 \quad (19)$$

These equations can then be analyzed for passive joint behaviors in response to commanded ones, without having to worry directly about the constraints or the fiber motion of the robot. Note that the *reduced shape mass matrix*  $\tilde{M}_b(b)$  is different from the reduced mass matrix of Equation (16). The equation components for the single passive joint case are shown in Appendix A.

We note here that the dynamics also allow us to consider additional noise such as wheel slip close to singular configurations. If the kinematics are indeed modeled by “soft” rather than “hard” constraints to allow for wheel slip on arbitrary links, then it would be possible to allow for more than three commanded joints. The realization of soft constraints will be considered in future work; here we extend our work on a three-link robot with one commanded joint (Dear et al., 2016a,b) to a multi-link robot with the same.

#### 4.1. Singular configuration

In our kinematic analysis of the multi-link robot, we have seen that singular configurations, i.e., those for which the constraints are angled such that at least one is rendered redundant, can be problematic for locomotion since they lead to large constraint forces. For the three-link case, a closer look at the connection from Equation (9) shows that

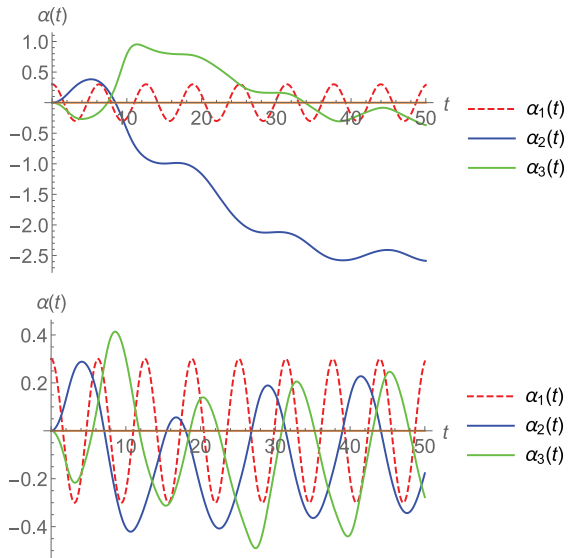
the denominator  $D$  goes to zero when  $\alpha_1(t_0) = \alpha_2(t_0)$  for some time  $t = t_0$ . In general, the robot will violate a non-holonomic constraint when passing through singular configurations; the exception to this implication is if we have the velocity condition  $\dot{\alpha}_1(t_0) = -\dot{\alpha}_2(t_0)$ , as we showed in Dear et al. (2016b). If this velocity condition is satisfied, the robot exhibits a hybrid behavior in which it enters a dynamic drifting state at  $t = t_0$ , followed by a transition back to a kinematic state after  $t = t_0$ .

Figure 12 shows how the above condition appears on the vector field representation of the  $\xi_x$  component of the connection (prior to conversion to a scalar function via the curl of the field, as shown in Figure 4). As stated previously, the singularity configurations occur along the line  $\alpha_1 = \alpha_2$ . In order for the robot to cross these configurations without violating any constraints, its joint velocities must satisfy  $\dot{\alpha}_1 = -\dot{\alpha}_2$ , an example of which is shown by the trajectory overlaid on the vector plot. On a physical robot, this condition need not be satisfied exactly, since the robot’s wheels can simply slip when passing through a singular configuration with arbitrary joint velocities.

Away from singularities, the line integral of the vector field along the trajectory provides us a measure of displacement along the body frame direction corresponding to the plotted field, as per Equation (11). For example, if the trajectory in Figure 12 were traversed in a clockwise direction, the line integral would increase nearly everywhere along the path, and the robot would acquire a positive displacement in the body’s forward direction. At the point where the path crosses  $\alpha_1 = \alpha_2$ , the corresponding vector has infinite magnitude. However, because the trajectory is such that  $\dot{\alpha}_1 = -\dot{\alpha}_2$ , it passes exactly perpendicularly to the vector field direction, allowing the line integral contribution and, thus, displacement to be identically zero.

Although the line integral approximation of body displacement is still valid with this configuration at the singularities, we can no longer do the full Stokes conversion of Equation (11) to an area integral if the trajectory passes through  $\alpha_1 = \alpha_2$ , even if we ensure that  $\dot{\alpha}_1 = -\dot{\alpha}_2$  at those points. This is because any closed trajectory passing through a singular configuration actually encloses two distinct areas, one on either side of the singularity line. Because area integrals over these types of shape space regions can be challenging to compute, we use the vector field line integrals for displacement approximations, but will continue to use the scalar curl functions for visual representation.

With regard to our dynamic model of locomotion, we know that with only one commanded joint input, the solution of Equation (19) for the remaining passive joint also satisfies  $\dot{\alpha}_1(t_i) = -\dot{\alpha}_2(t_i)$  if the solution contains singularity configurations at times  $t_i$ . As such gaits are symmetric about the origin of the joint space in the steady state, this allows for forward locomotion of the robot without net rotation, as we have seen from Figure 4. Figure 13 shows two simulated trajectories of a four-link robot, where  $\alpha_1(t) = 0.3 \cos(0.5t)$ . All parameters are assigned to a



**Fig. 13.** Top:  $\alpha_2$  and  $\alpha_3$  are completely passive joints, so that they can drift away from the origin. Bottom:  $\alpha_2$  and  $\alpha_3$  have stabilizing springs.

value of 1 in both, except the spring constant on the passive joints  $k_2$  and  $k_3$ , which are 0 in the first plot. Without stabilizing springs,  $\alpha_2$  is able to drift away from the origin and would, in fact, converge toward  $\pi$  if damping were also non-existent ( $d_2 = 0$ ), a situation detrimental to overall locomotion. In contrast, when  $k_2 = 1$  the passive joints exhibit stable oscillatory motions with amplitude and offset roughly equal to those of  $\alpha_1$ .

#### 4.2. Passive joint trajectories

Here we look exclusively at the problem of generating particular passive joint trajectories for a single-input multi-link robot, assuming stabilizing springs on the passive joints for stable oscillatory motions. In particular, we are interested in the response of the second joint  $\alpha_2$  (assuming the input is at the first joint  $\alpha_1$ ), because knowledge of the first two joint trajectories is sufficient to determine overall system locomotion. Assuming periodic inputs, we would like to be able to effect the shape and alignment of the closed gait in the  $\alpha_1$ - $\alpha_2$  joint space, as we know from the connection exterior derivative that the greatest area, and thus displacement, in the body  $x$  direction occurs close to and along the  $\alpha_1 = \alpha_2$  axis.

Assuming that we only have sinusoidal inputs, and therefore sinusoidal gaits, this allows us to narrow down our trajectories to only elliptical ones in the joint space. The alignment of such an ellipse, or whether it is wider or narrower along the  $\alpha_1 = \alpha_2$  direction, is therefore determined by the magnitude, phase, and offset parameters of the input joint, just as with our observations for the kinematic case in Section 3.1.3.

**4.2.1. Joint harmonics.** The first assertion that we will show is that the trajectory of  $\alpha_2$  tends to track that of  $\alpha_1$ , with the exception of a phase offset. In other words, suppose that we command a finite sinusoidal trajectory  $\alpha_1 : \mathbb{R}^+ \rightarrow B$  for a single-input  $m$ -link robot governed by Equation (19), where the remaining joints are all spring-loaded. Then the trajectory of the proximal passive joint  $\alpha_2$  will tend toward a phase-shifted version of  $\alpha_1$ , i.e.,  $\alpha_2(t) \rightarrow \alpha_1(t - \phi)$  for some finite  $\phi$  over time. The solution of this robot's nonlinear base dynamics thus produces sinusoidal shape trajectories given that  $\alpha_1$  is also sinusoidal.

For autonomous systems with a two-dimensional shape space, such solutions exist as limit cycles and can be analyzed using the Poincaré–Bendixson theorem, as described by Wiggins (2003), Guckenheimer and Holmes (2013), and Strogatz (2018). Burton et al. (2010) were able to analytically find limit cycle expressions for the passive orientation response of a two-link robotic swimmer given an input gait at its joint. However, our system cannot be simplified in the same way. An algebraic method that is applicable toward systems such as the multi-link snake robot is the *harmonic balance* method, presented and extended for various systems by authors such as Hayashi (2014), Mickens (1986), and Luo and Huang (2012). This can also be seen as an alternative to asymptotic analysis via perturbation expansion, used by Passov and Or (2012) to describe the dynamics of a three-link swimmer with a passive joint.

The general idea of harmonic balance, which we will use to show our assertion, is as follows. Instead of analyzing a nonlinear system of differential equations in the time domain, we transform it into a nonlinear system of algebraic equations in the frequency domain. The solution to the original differential equation, assumed to take a sinusoidal form, can be written as a Fourier series, or linear combination of harmonics, and the coefficients of the harmonics are algebraically solved by *balancing* the corresponding frequency domain component at each harmonic. It may not always be possible to find exact solutions for all the chosen harmonics, particularly since in practice the series representation of the solution is truncated when an infinite series is required. However, the error in the difference is an indicative measure of the goodness of fit.

What we will do here is assume a general sinusoidal input  $\alpha_1(t) = A_1 + B_1 \cos(\omega t)$ . In the method of harmonic balance, the passive joint  $\alpha_2(t)$  then follows a trajectory described by the Fourier series

$$\alpha_2(t) = A_2 + \sum_{k=1}^N B_{2,k} \cos(k\omega t) + C_{2,k} \sin(k\omega t) \quad (20)$$

Here, the order  $N$  of the series is often chosen to replicate the system response as closely as possible. A general system may have an infinite number of harmonics, but from simulations of our robot we observe that only the first

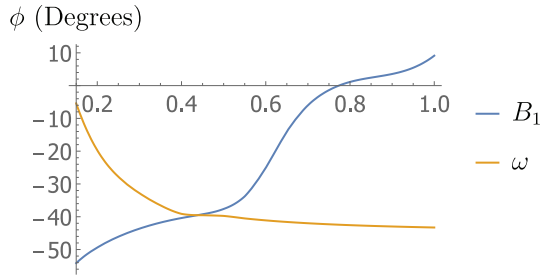


**Fig. 14.** An example of the phase of the passive  $\alpha_2$  joint over a sweep of input amplitudes  $B_1$  (where  $\alpha_1(t) = B_1 \cos(0.3t)$ ) and frequencies  $\omega$  (where  $\alpha_1(t) = 0.3 \cos(\omega t)$ ). We note that we specifically chose to show the same numerical domains of the two parameters. These functions are numerically computed using the harmonic balance equations.

harmonic (the same frequency as that of the input) is prevalent. If we choose to expand the series to higher-order harmonics we would find that the corresponding coefficients are orders of magnitude smaller.

We thus choose  $N = 1$  and substitute both  $\alpha_1(t)$  and  $\alpha_2(t)$  and their time derivatives into Equation (19). As the dynamics contain trigonometric terms in  $\alpha_1$  and  $\alpha_2$ , which are themselves trigonometric and contain the coefficients to be solved (refer to Appendix A for the analytical forms), we expand these functions using a Taylor approximation up to third order. However, we leave the joint trajectories as exact sinusoidal functions of  $t$ , giving us an equation that is a linear combination of harmonics in  $\cos(\omega t)$ ,  $\sin(\omega t)$ ,  $\cos(2\omega t)$ ,  $\sin(2\omega t)$ , and so on; higher-order harmonics appear from products of first-order ones. Each harmonic term yields an individual algebraic equation for the coefficients in front of the harmonics, giving us a system of three equations in the three unknowns  $A_2$ ,  $B_{2,1}$ , and  $C_{2,1}$ .

We find that our equations are too complex to solve analytically, so for this article we only present some numerical results for various combinations of input parameters. In general, we observe that the offset  $A_2$  generally tracks the input offset  $A_1$ . The coefficients  $B_{2,1}$  and  $C_{2,1}$  determine the magnitude and phase of  $\alpha_2$ . Our numerical solutions show that the magnitude

$\sqrt{(B_{2,1})^2 + (C_{2,1})^2}$  is approximately equal to  $B_1$ .

For robots with more than three links, the observation that the  $\alpha_2$  joint, and indeed each of the remaining passive joints, is simply phase-shifted from the joint prior to it still holds true. In applying the method of harmonic balance, we would have equivalent Fourier series representations, analogous to Equation (20), for each of the passive joints. The number of unknowns, and correspondingly algebraic equations, then increases linearly with the number of additional links.

**4.2.2. Joint phase.** In the harmonic balance equations above, the unknown coefficients of the passive response  $\alpha_2$  are solved via nonlinear equations in the known parameters

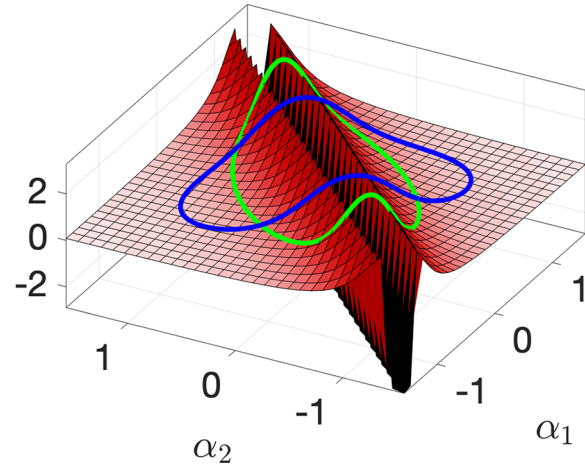


**Fig. 15.** Two gaits of a four-link snake robot with a commanded  $\alpha_1$  joint and passive  $\alpha_2$ . The gait with a phase of  $150^\circ$  (blue) acquires less displacement per cycle than the one with a phase of  $80^\circ$  (green).

Note: Please refer to the online version for colour figure.

of the input. Specifically, the values  $B_{2,1}$  and  $C_{2,1}$  change as functions of the input amplitude  $B_1$  and frequency  $\omega$ , and different value combinations of  $B_{2,1}$  and  $C_{2,1}$  then determine the resultant phase shift of the trajectory of  $\alpha_2$  from  $\alpha_1$ .

While the harmonic balance equations are not very insightful and too lengthy to write out, we can visually show how the phase shift changes as functions of input amplitude and frequency. Figure 14 shows the variation in phase as functions of magnitude and frequency, where the inputs are  $\alpha_1(t) = B_1 \cos(0.3t)$  in the former and  $\alpha_1(t) = 0.3 \cos(\omega t)$  in the latter. These results are also useful for locomotion when viewed from a geometric perspective. We see that, in general, phase increases as input magnitude increases or as input frequency decreases. Significantly, certain ranges of the amplitude  $B_1$  cause the phase to tend to zero, which would lead to suboptimal or no locomotion. Such parameter combinations must be avoided.

Despite the robot having more than three links and only one commanded joint, the connection equation of Equation (4) and the associated connection exterior plots of Figure 4 are still valid descriptions of the robot. In other words, periodic gaits in the  $\alpha_1$ - $\alpha_2$  space overlaid on those plots give us a qualitative measure of the forward and turning displacement that the robot experiences when executing the corresponding  $\alpha_1$  input and experiencing the passive  $\alpha_2$  response. Figure 15 shows two such gaits for a four-link robot, one with a phase of  $150^\circ$  (blue) and the other  $80^\circ$  (green), overlaid on the  $x$  component of the connection exterior derivative. For the same input magnitude, the latter is able to acquire significantly more displacement per cycle, as it is more aligned with the  $\alpha_1$ - $\alpha_2$  axis.

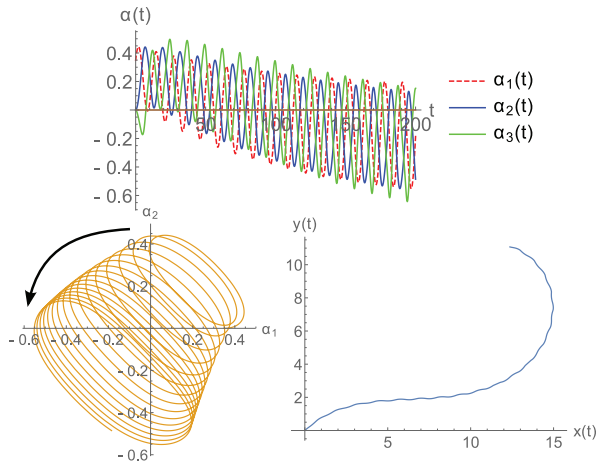


**Fig. 16.** Top: Feedback-controlled trajectory of  $\alpha_1$  and passive responses of  $\alpha_2$  and  $\alpha_3$ . Bottom left: The trajectory in  $\alpha_1$ - $\alpha_2$  space. Bottom right: The robot's fiber trajectory.

### 4.3. Stabilizing feedback controller

As the system can pass through singular configurations, a stabilizing feedback controller can be more easily defined than in the kinematic case. In the previous subsection we showed how the phase shift between  $\alpha_1$  and  $\alpha_2$  can be varied according to the parameters of the input gait. In addition, we reviewed how the resultant shape space representation of the gait in  $\alpha_1$ - $\alpha_2$  space gives us a geometric interpretation of the robot's locomotion.

In addition to changing the passive joints' phase offset, the balance equations also show that those joints' magnitude and offset generally follow those of the commanded joint. This is sufficient for achieving arbitrary fiber motions on the plane, because we can use the kinematic model of geometric phase to approximate gaits that will mainly move the robot forward in the same body direction (centered about the origin), or those that turn the robot in a specific direction (offsetting the gait away from the origin). Feedback controllers, as described for the kinematic model, can then be imposed on the magnitude and offset of the input  $\alpha_1$  in order to achieve the same desired values for the passive joints. The net effect is to shift and shape the trajectory along the  $\alpha_1 = \alpha_2$  line in the first two dimensions of the joint space in order to achieve a desired displacement and reorientation per cycle.

Figure 16 shows an example of this controller applied to a four-link robot. The joint trajectories initially start centered around 0.2 radians, with a magnitude about the same. These are the loops centered around the first quadrant of the joint space plot (bottom left). The input frequency was chosen such that the resulting phase is about a third of a gait cycle. According to the exterior derivative plot for  $\theta$  in Figure 4, the robot follows a trajectory of slightly negative curvature and with a small forward displacement per gait cycle (bottom right). It is then desired for the robot to start turning more sharply in the opposite direction: this

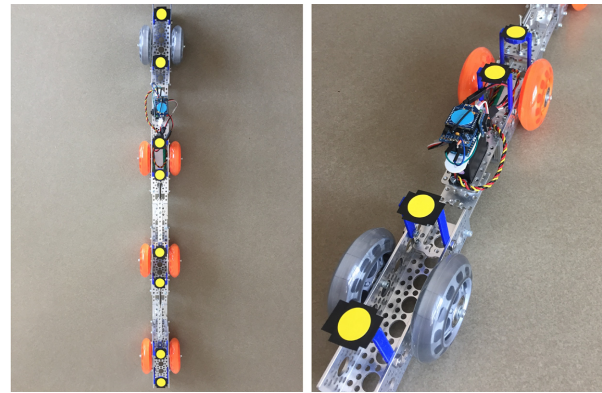


**Fig. 17.** Left: Top view of an experimental four-link robot, actuated by one joint with a servo motor and the rest passively compliant. Right: Closeup of the first two links and servo joint.

corresponds to shifting the gait downward to the third quadrant in  $\alpha_1$ - $\alpha_2$  space and increasing its magnitude. As shown in the top plot, this is achieved by increasing the magnitude and decreasing the offset of  $\alpha_1$  over time, causing both  $\alpha_2$  and  $\alpha_3$  to follow.

This controller design can be applied to robots with an arbitrary number of links. The passive joint trajectories will change because the presence of additional joints down the line couple into their dynamics. However, the commanded joint can still use feedback to shape the adjacent joint, followed by the remaining ones down the chain, with each successive one down the chain following its predecessor.

## 5. Experimental results

To verify some of our theoretical observations and analyses, experimental apparatuses resembling the three- and four-link non-holonomic snake robot models are used to qualitatively assess gait, joint-angle, and workspace trajectories. To facilitate easy development of different and modular configurations, we use prefabricated parts from Actobotics as the primary source of components for the robot. A physical realization of a four-link robot with a single commanded input joint and passively compliant joints is shown in Figure 17.

We use skate wheels made of polyurethane with standard ball bearings to realize the single wheel shown in the model. Note that while each link contains two wheels instead of one, the non-holonomic constraint on a single wheel is identical to those acting on the two wheels on each link in the experiments. Linear springs are used to model passive compliance. By attaching one end of the spring to a lever arm extended over a joint and the other end to the neighboring link, the spring can undergo linear deflections. The lever arm thus experiences a force similar to that of a torsional spring. An example of the configuration of each spring is shown in Figure 18.

The modular nature of our system easily allows for the robot to contain an arbitrary number of links, from three to

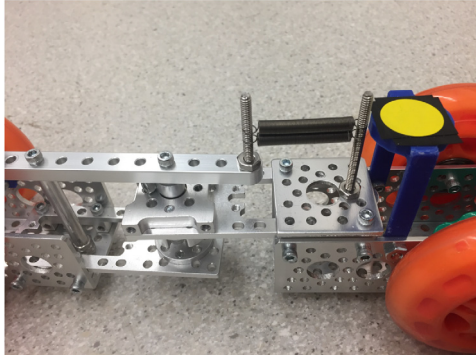


**Fig. 18.** Detail of the linear spring implementation between the passive joints of the robot. The effective stiffness can vary in the number of springs used.

four or more. Each link is about 6 inches long and connects to neighboring links using identical parts for consistency and symmetry. The total lengths of the three- and four-link robots are about 24 inches and 33.5 inches, respectively. At the proximal input joint, the robot is equipped with an Adafruit Pro Trinket to control a servo motor. Communications and power are handled via an XBee Series 1 wireless communication module and a 6 V, 350 mAh NiMH battery.

Tracking of the robot is done via the position and orientation of each individual robot link, atop which is affixed two yellow markers equidistant from the center of the link. These markers' trajectories are tracked relative to the laboratory frame, which is defined also by four yellow markers placed at the corners of the general workspace area.

We capture video using a Raspberry Pi and Pi camera and postprocess these videos using MATLAB, in which the positions of each marker are identified and recorded on a frame-by-frame basis. These positions determine the centroid and, thus, position of each link relative to the laboratory frame. Link orientations are determined using relative measurements between neighboring links. In all experiments, the orientation and trajectory of the robot relative to the laboratory frame are computed using the second link. The Raspberry Pi and Pi camera are mounted 10 feet above the workspace providing an effective area approximately 6 feet wide and 10 feet long. Figure 19 shows a perspective of the workspace and the previously described components, along with the four-link robot in the space.

### 5.1. Parameter sweeps

In Section 4.2, we observed that the relative phase of the robot's first two joint trajectories generally varies with both the amplitude and the frequency of the sinusoidal input. We perform sweeps in both parameters to show that the experimental robot exhibits qualitatively similar behavior. From our geometric understanding of the system, we also know that the relative phase directly affects locomotive efficiency,

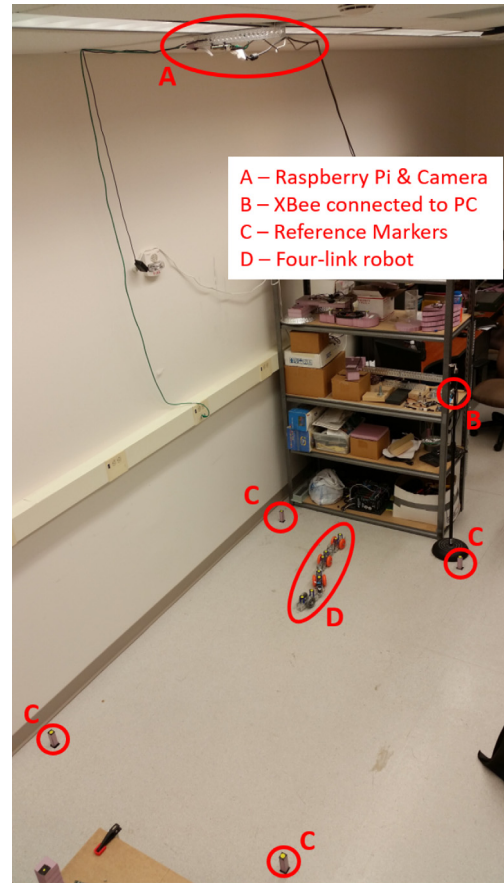


**Fig. 19.** The experimental setup with camera and markers, along with the four-link robot in the workspace.

measured by displacement per gait cycle per amplitude. This relationship can be visually understood by the alignment of the closed loop in  $\alpha_1$ - $\alpha_2$  space.

Figure 20 shows an amplitude sweep for a three-link robot, where the amplitude of the input trajectory varies from  $20^\circ$  to  $70^\circ$  while the frequency is kept constant at 0.3 Hz. As expected, the phase depiction of the gaits in the shape space shows the ellipses moving from alignment with the  $-\alpha_1$ - $\alpha_2$  diagonal to alignment with the  $\alpha_1$ - $\alpha_2$  diagonal. Such a transition in the gait phase, as well as the fact that the subsequent experiments have a higher magnitude per gait cycle, results in the robot obtaining a higher displacement per cycle in the latter experiments. The workspace trajectories are shown side by side in the second plot of Figure 20; they are placed at regular intervals along the  $y$  axis and reoriented such that the second link is aligned with the laboratory  $x$  axis. Note that at  $70^\circ$  the workspace trajectory actually starts to turn away from its original heading. This is not surprising as large swings of the robot's links are prone to incur unmodeled effects such as slipping and resistance against neighboring links.

Similarly, Figure 21 depicts a frequency sweep, where the frequency of the input varies from 0.2 to 1 Hz while the amplitude is kept constant at  $55^\circ$ . As frequency increases,

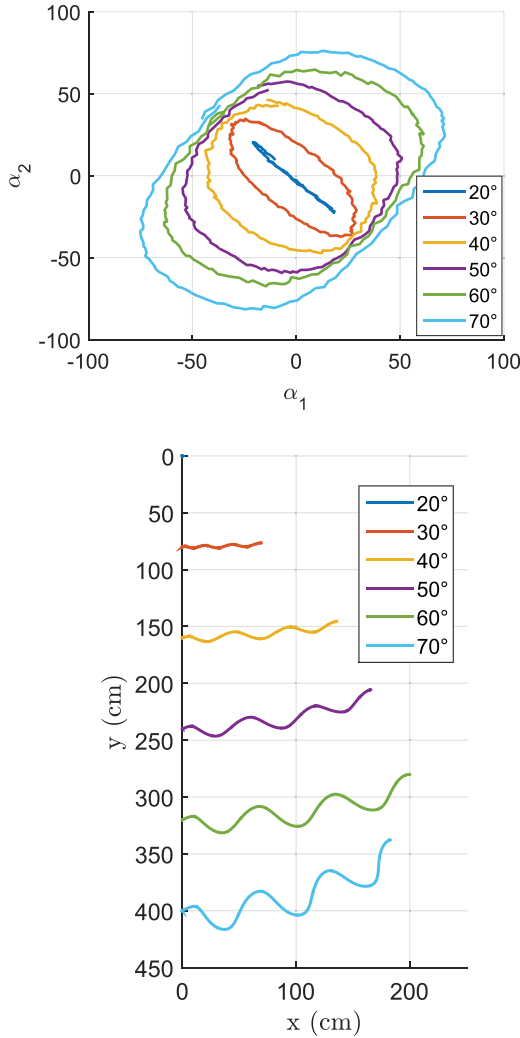


**Fig. 20.** Shape space (top) and workspace (bottom) trajectories of a three-link robot undergoing an amplitude sweep ranging from  $20^\circ$  to  $70^\circ$  for the commanded  $\alpha_1$  joint at frequency 0.3 Hz.

the shape space depiction of the gait becomes more anti-aligned with the positive  $\alpha_1$ - $\alpha_2$  diagonal. As amplitude remains the same in each instance (i.e., the path length of the shape space representation remains almost constant), we can fairly compare the effect of the relative gait phase on overall displacement, and we see that anti-alignment produces markedly less displacement per cycle than alignment with the  $\alpha_1$ - $\alpha_2$  diagonal. We also have simulation sweep results as a point of comparison for the experiments in Figure 22; although the values of the frequencies and amplitudes are different owing to parameter tuning, we see that qualitatively our model predicts the robot's trajectories very well. Finally, observed values for the mean forward speed and net displacement, as well as phase shift between the two joint trajectories, for both sets of experiments are summarized in Table 1.

In the previous experiments, the offset of the sinusoidal input is zero, resulting in a mostly straight workspace trajectory aligned with the robot's initial heading. As we recall

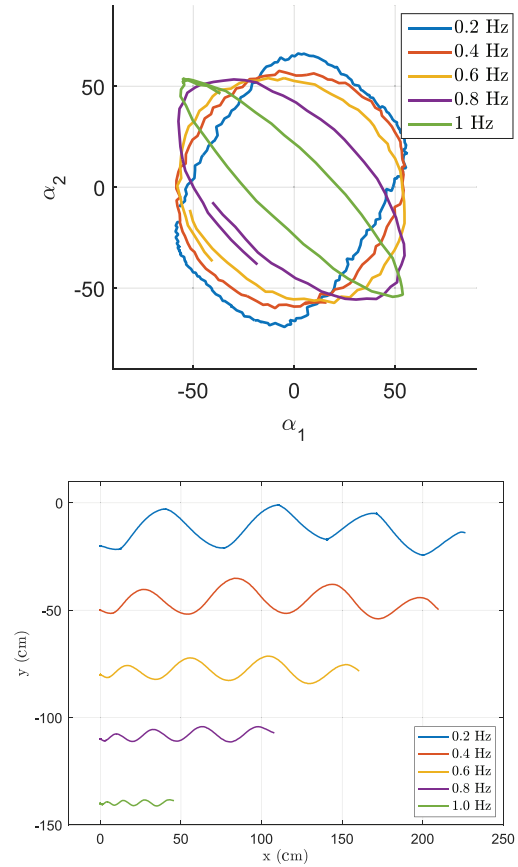


**Fig. 21.** Shape space (top) and workspace (bottom) trajectories of a three-link robot undergoing a frequency sweep ranging from 0.2 to 1 Hz for the commanded  $\alpha_1$  joint at amplitude  $55^\circ$ .

from the equation corresponding to the  $\theta$  component of the robot's body velocity, as well as the corresponding exterior derivative plot in Figure 4, a non-zero offset will introduce a non-zero curvature to the robot's trajectory. Figure 23 shows that by introducing an offset into the input, the passive joint will track this offset as well. The offset of the commanded joint  $\alpha_1$  is continuously increased from the beginning of the experiment, resulting in the workspace trajectory having an increasing curvature.

## 5.2. Navigation

As described in Section 4.3, it is possible to use our knowledge about the dependence of workspace displacement and trajectory curvature on the robot's input parameters to conduct navigation of the environment. For greater displacement per cycle, the robot commands the input joint to either increase amplitude or decrease frequency until the desired velocity is achieved. To turn around, the input must acquire a non-zero offset, with the sign of the offset determining the turn direction. For this experiment, we introduce an obstacle along the robot's unmodified trajectory and precompute suitable trajectory segments that would allow the robot to navigate around it. These segments are

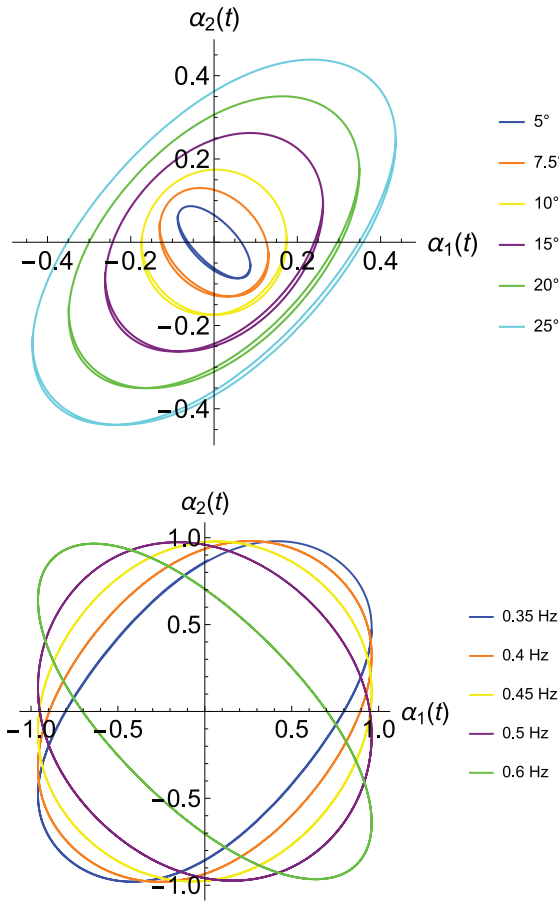


**Fig. 22.** Amplitude (top) and frequency (bottom) shape space trajectories obtained from simulation. They are qualitatively very similar to the experimental results obtained in Figures 20 and 21.

**Table 1.** Observed mean forward speed, net displacement, and phase shift for the amplitude and frequency sweep experiments.

Amplitude (deg)	Mean forward speed (cm/s)	Net displacement (cm)	Phase shift (s)
20	0	0	0
30	4.80	85.4	1.43
40	9.84	160	0.976
50	13.7	212	0.857
60	21.8	215	0.762
70	21.7	220	0.740
Frequency (Hz)	Mean forward speed (cm/s)	Net displacement (cm)	Phase shift (s)
0.2	13.4	227	1.10
0.4	14.3	220	0.666
0.6	16.8	182	0.523
0.8	16.2	132	0.405
1.0	8.54	59.7	0.452

then stitched together via smoothing functions to obtain a continuous input command. The resulting shape space depiction of  $\alpha_1$  and  $\alpha_2$ , as well as the trajectory taken by the robot, are shown in Figure 24.

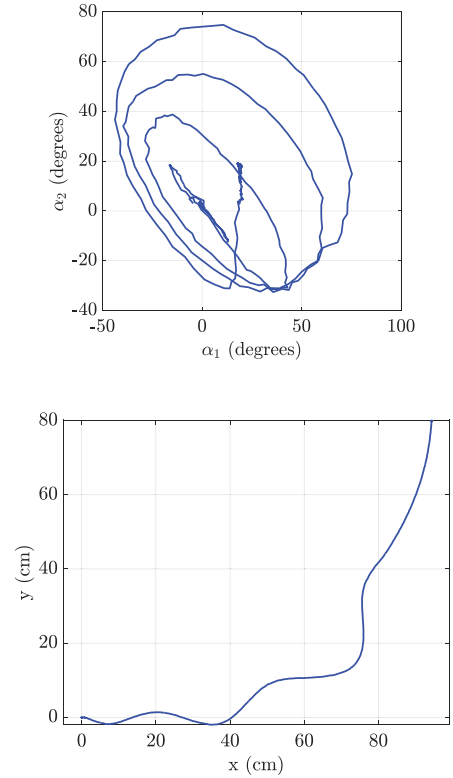


**Fig. 23.** Shape space (top) and workspace (bottom) trajectories of a four-link robot continuously varying its input offset parameter. When the commanded joint  $\alpha_1$  acquires an offset, the workspace trajectory has non-zero curvature.

## 6. Conclusions and future work

We have developed and studied kinematic and dynamic models for a  $m$ -link fully non-holonomic snake robot. With the kinematic model we showed that the joint kinematics take on a chained form, allowing us to determine gaits with two adjacent or non-adjacent joints that can avoid locked and singular configurations. We also characterized oscillatory modes for the passive joints that qualitatively inform a class of feedback controllers. The dynamic model, though more complex, allows for elements such as stabilizing torsional springs and locomotion of the robot by actuating only one joint. The method of harmonic balance provided an approximate solution to the robot's dynamics that allowed us to characterize the phase response of the passive joints, which were then connected to geometric phase analysis in order to describe the robot's motion. Finally, we were able to show some of our analyses on a three- and four-link robot, as well as primitive navigation results.

Further quantitative analysis is necessary for proving that some of our observations presented here are, in fact, general. For example, in the kinematic case of two controlled joints, it may be possible to cleverly turn different combinations of joints on and off to achieve different desired configurations of the remaining joints. This would

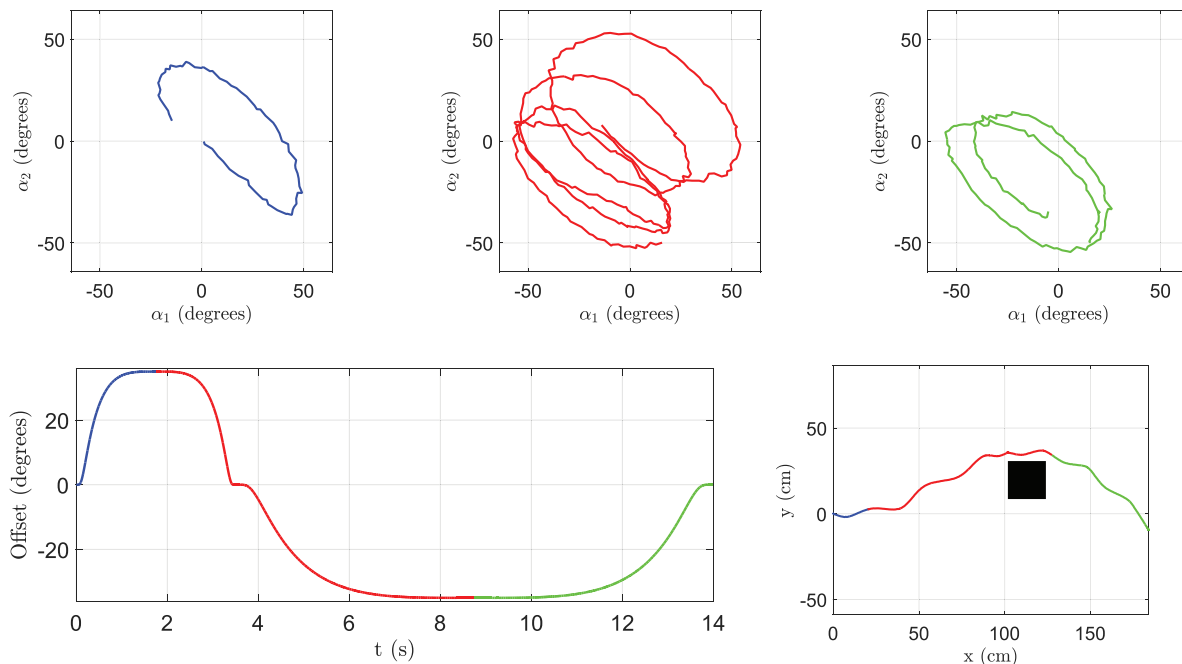


**Fig. 24.** Top: Three shape-space segments of a full trajectory of a four-link robot modulating the offset of its input joint  $\alpha_1$ . Starting at the origin, the robot has a positive offset, leading to initial orientation to its left. The second segment is a transition to a negative offset in order to zero out the workspace curvature. The last segment smoothly increases the offset back to zero. Bottom left: Value of the input joint's offset over time, colored into three different segments corresponding to the gait segments in the shape spaces above. Bottom right: Resultant workspace trajectory of the four-link robot navigating around an obstacle.

involve a more thorough investigation of how the passive joint responses change in the adjacent and non-adjacent commanded cases, as well as how to provably avoid locking configurations.

Going forward we would like to derive more sophisticated controllers and locomotion maneuvers. In our dynamic analysis, the gaits that we considered are sufficient to propel and orient the robot in arbitrary directions, but they have all emerged to be symmetric about one of the shape space diagonals (i.e., they cross singularities). While offset gaits such as those of the kinematic model may not necessarily provide new locomotion modes, it may be interesting to see whether a greater variety of gaits can indeed be induced. For example, one can propose a trajectory with a variety of turns and curves and then quantify the effectiveness of a simple feedback controller in enabling the robot to follow it. Finally, we would like to explore additional dynamic elements added to the robot, such as wheel slip or lateral friction, which would likely be more faithful to a physical system. By “softening” the constraints we can then extend our work to analogous kinematic systems such as a low- or high-Reynolds-number swimmer snake robot.

### Funding

This research received no specific grant from any funding agency in the public, commercial, or not-for-profit sectors.

### Notes

1. We plot a scaled arctangent of these functions in order to visualize the singular portions. Instead of  $dA_j(b)$ , we plot  $1/k \arctan(k dA_j(b))$ , where  $k$  is positive.

### ORCID iD

Tony Dear  <https://orcid.org/0000-0001-5780-3240>

### References

- Abraham R, Marsden JE and Marsden JE (1978) *Foundations of Mechanics*, Vol. 36. Reading, MA: Benjamin/Cummings Publishing Company.
- Altafini C, Speranzon A and Wahlberg B (2001) A feedback control scheme for reversing a truck and trailer vehicle. *IEEE Transactions on robotics and automation* 17(6): 915–922.
- Bloch A, Baillieul J, Crouch P, et al. (2003) *Nonholonomic Mechanics and Control*, Vol. 24. Berlin: Springer.
- Bullo F and Lynch KM (2001) Kinematic controllability for decoupled trajectory planning in underactuated mechanical systems. *IEEE Transactions on Robotics and Automation* 17(4): 402–412.
- Burton L, Hatton RL, Choset H and Hosoi A (2010) Two-link swimming using buoyant orientation. *Physics of Fluids* 22(9): 091703.
- Dear T, Kelly SD, Travers M and Choset H (2016a) Locomotive analysis of a single-input three-link snake robot. In: *2016 IEEE 55th Conference on Decision and Control (CDC)*, pp. 7542–7547.

- Dear T, Kelly SD, Travers M and Choset H (2016b) The three-link nonholonomic snake as a hybrid kinodynamic system. In: *2016 American Control Conference (ACC)*, pp. 7269–7274.
- Dear T, Kelly SD, Travers M and Choset H (2017) Locomotion of a multi-link nonholonomic snake robot. In: *ASME 2017 Dynamic Systems and Control Conference*. American Society of Mechanical Engineers.
- Guckenheimer J and Holmes P (2013) *Nonlinear Oscillations, Dynamical Systems, and Bifurcations of Vector Fields*, Vol. 42. Springer Science & Business Media.
- Hatton RL and Choset H (2011) Geometric motion planning: The local connection, Stokes' theorem, and the importance of coordinate choice. *The International Journal of Robotics Research* 30(8): 988–1014.
- Hayashi C (2014) *Nonlinear Oscillations in Physical Systems*. Princeton, NJ: Princeton University Press.
- Hirose S (1993) *Biologically Inspired Robot*. Oxford: Oxford University Press.
- Kelly SD and Murray RM (1995) Geometric phases and robotic locomotion. *Journal of Robotic Systems* 12(6): 417–431.
- Krishnaprasad PS and Tsakiris DP (1994) G-snakes: Nonholonomic kinematic chains on lie groups. In: *Proceedings of the 33rd IEEE Conference on Decision and Control*, Vol. 3. IEEE, pp. 2955–2960.
- Luo AC and Huang J (2012) Approximate solutions of periodic motions in nonlinear systems via a generalized harmonic balance. *Journal of Vibration and Control* 18(11): 1661–1674.
- Marsden JE, Montgomery R and Ratiu TS (1990) *Reduction, Symmetry, and Phases in Mechanics*, Vol. 436. Providence, RI: American Mathematical Society.
- Matsuno F and Mogi K (2000) Redundancy controllable system and control of snake robots based on kinematic model. In: *Proceedings of the 39th IEEE Conference on Decision and Control*, Vol. 5. IEEE, pp. 4791–4796.
- Matsuno F and Sato H (2005) Trajectory tracking control of snake robots based on dynamic model. In: *Proceedings of the 2005 IEEE International Conference on Robotics and Automation, 2005 (ICRA 2005)*. IEEE, pp. 3029–3034.
- Matsuno F and Suenaga K (2003) Control of redundant 3D snake robot based on kinematic model. In: *Proceedings IEEE International Conference on Robotics and Automation, 2003 (ICRA'03)*, Vol. 2. IEEE, pp. 2061–2066.
- Mickens R (1986) A generalization of the method of harmonic balance. *Journal of Sound and Vibration* 111(3): 515–518.
- Mukherjee R and Anderson DP (1993) Nonholonomic motion planning using Stoke's theorem. In: *Proceedings 1993 IEEE International Conference on Robotics and Automation*. IEEE, pp. 802–809.
- Murray RM and Sastry SS (1993) Nonholonomic motion planning: Steering using sinusoids. *IEEE Transactions on Automatic Control* 38(5): 700–716.
- Ostrowski J (1999) Computing reduced equations for robotic systems with constraints and symmetries. *IEEE Transactions on Robotics and Automation* 15(1): 111–123.
- Ostrowski J and Burdick J (1996) Gait kinematics for a serpentine robot. In: *Proceedings 1996 IEEE International Conference on Robotics and Automation*, Vol. 2, pp. 1294–1299.
- Ostrowski J and Burdick J (1998) The geometric mechanics of undulatory robotic locomotion. *The International Journal of Robotics Research* 17(7): 683–701.
- Ostrowski JP, Desai JP and Kumar V (2000) Optimal gait selection for nonholonomic locomotion systems. *The International Journal of Robotics Research* 19(3): 225–237.
- Passov E and Or Y (2012) Dynamics of Purcell's three-link microswimmer with a passive elastic tail. *The European Physical Journal E* 35(8): 1–9.
- Pratsch P and Mita T (1999) Control and analysis of the gait of snake robots. In: *Proceedings of the 1999 IEEE International Conference on Control Applications*, Vol. 1. IEEE, pp. 502–507.
- Pratsch P, Mita T and Iwasaki T (2000) Analysis and control of a gait of snake robot. *IEEE Transactions on Industry Applications* 120(3): 372–381.
- Shammas EA, Choset H and Rizzi AA (2007) Geometric motion planning analysis for two classes of underactuated mechanical systems. *The International Journal of Robotics Research* 26(10): 1043–1073.
- Shapere A and Wilczek F (1989) Geometry of self-propulsion at low Reynolds number. *Journal of Fluid Mechanics* 198: 557–585.
- Strogatz SH (2018) *Nonlinear Dynamics and Chaos: With Applications to Physics, Biology, Chemistry, and Engineering*. Boca Raton, FL: CRC Press.
- Tanaka M and Tanaka K (2016) Singularity analysis of a snake robot and an articulated mobile robot with unconstrained links. *IEEE Transactions on Control Systems Technology*. DOI: 10.1109/TCST.2016.2528888.
- Wiggins S (2003) *Introduction to Applied Nonlinear Dynamical Systems and Chaos*, Vol. 2. Springer Science & Business Media.
- Ye C, Ma S, Li B and Wang Y (2004) Locomotion control of a novel snake-like robot. In: *Proceedings 2004 IEEE/RSJ International Conference on Intelligent Robots and Systems, 2004 (IROS 2004)*, Vol. 1, pp. 925–930.
- Yona T and Or Y (2019) The wheeled three-link snake model: Singularities in nonholonomic constraints and stick-slip hybrid dynamics induced by Coulomb friction. *Nonlinear Dynamics* 95(3): 2307–2324.

## Appendix. Dynamics of base variables

We present here the analytical forms of the base dynamics equation (Equation (19)) for a robot with two joints  $b = (\alpha_1, \alpha_2)^T$ , link length  $R$ , identical link masses  $M^l$ , and identical joint masses  $M^j$ . Only  $\alpha_2$  is passive, so we have one equation

$$0 = (\tilde{M}_{b1} \quad \tilde{M}_{b2}) \ddot{b} + \tilde{C}(b, \dot{b}) + \tilde{K}(b)$$

where

$$\begin{aligned} \tilde{M}_{b1} &= \frac{4 \cos^2 \frac{\alpha_2}{2}}{\cos^2 \frac{\alpha_1}{2}} ((M^l R^2 - 4J) \cos \frac{1}{2}(\alpha_1 - 3\alpha_2) + \\ &\quad (12J + (3M^j + 2M^l)R^2 + (2M^l R^2 - 8J) \cos \alpha_1) \\ &\quad \times \cos \frac{1}{2}(\alpha_1 - \alpha_2)) \end{aligned}$$

$$\begin{aligned} \tilde{M}_{b2} &= -4(4J - M^l R^2)(2 \cos \alpha_1 + \cos(\alpha_1 - 2\alpha_2)) \\ &\quad + 48J + 4(3M^l + 2M^j)R^2 \end{aligned}$$

$$\begin{aligned} \tilde{C} &= 128d_2 \dot{\alpha}_2 \cos^2 \frac{\alpha_2}{2} \sin^2 \frac{1}{2}(\alpha_1 - \alpha_2) \\ &\quad + \frac{2\alpha_1 \dot{\alpha}_2}{\cos^2 \frac{\alpha_1}{2}} (-M^l R^2 (\sin \frac{3\alpha_1}{2} + \sin \frac{1}{2}(\alpha_1 - 4\alpha_2)) \\ &\quad + 2(8J + M^j R^2) \sin \frac{\alpha_1}{2} - 8J \sin \frac{1}{2}(\alpha_1 - 2\alpha_2)) \\ &\quad + \frac{2\dot{\alpha}_2^2 \cos^2 \frac{1}{2}(\alpha_1 - 2\alpha_2)}{\cos^2 \frac{\alpha_2}{2} \sin^2 \frac{1}{2}(\alpha_1 - \alpha_2)} (8J + 2(2M^l + M^j)R^2 \end{aligned}$$

$$\begin{aligned}
& + (4J - M^l R^2)(\cos(\alpha_1 - \alpha_2) - 2\cos\alpha_1 - \cos\alpha_2)) \\
& - \frac{\dot{\alpha}_1^2 \cos\frac{1}{2}\alpha_2}{\cos^2\frac{\alpha_1}{2} \sin^2(\alpha_1 - \alpha_2)} ((3M^l R^2 - 8J) \cos\frac{3\alpha_1}{2} \\
& - M^l R^2 \cos\frac{\alpha_1 - 4\alpha_2}{2} + M^l R^2 \cos\frac{3\alpha_1 - 4\alpha_2}{2} \\
& + M^l R^2 \cos\frac{3\alpha_1 - 2\alpha_2}{2} + 2M^j R^2 \cos\frac{3\alpha_1 - 2\alpha_2}{2} \\
& + M^l R^2 \cos\frac{\alpha_1 - 2\alpha_2}{2} - M^l R^2 \cos\frac{5\alpha_1 - 2\alpha_2}{2}
\end{aligned}$$

$$\begin{aligned}
& + (12J + (7M^l + 2M^j)R^2) \cos\frac{\alpha_1}{2} \\
& + 8J \sin\frac{\alpha_1}{2} (\sin\alpha_2 - 3\sin(\alpha_1 - \alpha_2)) \\
& - 4J \cos\frac{3\alpha_1 - \alpha_2}{2}), \\
\tilde{K} & = 128k_2\alpha_2 \cos^2\frac{\alpha_2}{2} \sin^2\frac{1}{2}(\alpha_1 - \alpha_2)
\end{aligned}$$